Characteristics of Generating Cells in Wintertime Orographic Clouds

SARAH A. TESSENDORF,[a] KYOKO IKEDA,[a] ROY M. RASMUSSEN,[a] JEFFREY FRENCH,[b] ROBERT M. RAUBER,[c] ALEXEI KOROLEV,[d] LULIN XUE,[a] DEREK R. BLESTRUD,[e] NICHOLAS DAWSON,[e] MELINDA MEADOWS,[e] MELVIN L. KUNKEL,[e] AND SHAUN PARKINSON[e]

[a] *Research Applications Laboratory, National Center for Atmospheric Research, Boulder, Colorado*
[b] *Department of Atmospheric Sciences, University of Wyoming, Laramie, Wyoming*
[c] *Department of Climate, Meteorology, and Atmospheric Sciences, University of Illinois Urbana–Champaign, Urbana, Illinois*
[d] *Environment and Climate Change Canada, Toronto, Ontario, Canada*
[e] *Idaho Power Company, Boise, Idaho*

(Manuscript received 22 February 2023, in final form 14 December 2023, accepted 15 December 2023)

ABSTRACT: During the Seeded and Natural Orographic Wintertime clouds: the Idaho Experiment (SNOWIE) field campaign, cloud-top generating cells were frequently observed in the very high-resolution W-band airborne cloud radar data. This study examines multiple flight segments from three SNOWIE cases that exhibited cloud-top generating cells structures, focusing on the in situ measurements inside and outside these cells to characterize the microphysics of these cells. The observed generating cells in these three cases occurred in cloud tops of −15° to −30°C, with and without overlying cloud layers, but always with shallow layers of atmospheric instability observed at cloud top. The results also indicate that liquid water content, vertical velocity, and drizzle and ice crystal concentrations are greater inside the generating cells compared to the adjacent portions of the cloud. The generating cells were predominantly <500 m in horizontal width and frequently exhibited drizzle drops coexisting with ice. The particle imagery indicates that ice particle habits included plates, columns, and rimed and irregular crystals, likely formed via primary ice nucleation mechanisms. Understanding the sources of natural ice formation is important to understanding precipitation formation in winter orographic clouds, and is especially relevant for clouds that may be targeted for glaciogenic cloud seeding as well as to improve model representation of these clouds.

SIGNIFICANCE STATEMENT: This study presents the characteristics of cloud-top generating cells in winter orographic clouds, and documents that fine-scale generating cells are ubiquitous in clouds over complex terrain in addition to having been observed in other types of clouds. The generating cells exhibited enhanced concentrations of larger drizzle and ice particles, which suggests the environments of these fine-scale features promote ice formation and growth. The source of ice formation in winter clouds is critical to understanding and modeling the precipitation formation process. Given the ubiquity of cloud-top generating cells in many types of clouds around the world, this study further motivates the need to investigate methods for representing subgrid-scale environments to improve ice formation in numerical models.

KEYWORDS: Clouds; Orographic effects; Subgrid-scale processes; Cloud microphysics; Aircraft observations; Radars/Radar observations

1. Introduction

The formation of ice is a key microphysical process that contributes to precipitation production via ice-phase (Bergeron–Findeisen–Wegener; Wegener 1911; Bergeron 1935; Findeisen 1938) precipitation growth processes. Ice can form via primary nucleation either homogeneously at temperatures colder than −40°C or heterogeneously on ice nucleating particles (INP) at warmer (yet subfreezing) temperatures (Pruppacher and Klett 1997). Ice has also been shown to form via secondary processes that have been defined to occur after ice is already present or while ice is forming via primary methods (Hallett and Mossop 1974; Field et al. 2017; Korolev and Leisner 2020). Historically, primary ice nucleation was parameterized in models based on cloud temperature and supersaturation with respect to ice (Fletcher 1962; Meyers et al. 1992); however, DeMott et al. (2010) showed that these predictions of ice formation did not match observed concentrations. They proposed a parameterization for heterogeneous ice formation that was a function of temperature and INP concentration, whereas the latter was estimated based on the concentration of aerosol particles >0.5 μm. This new relationship substantially reduced the error of the previous temperature-based parameterizations from a factor of 1000 to within a factor of 10 (DeMott et al. 2010). The factor of 10 remaining scatter in the relationship was suggested to be caused by variability in the chemical composition of the INP. In this study we suggest that much of this variability may be due to the presence of generating cells.

Generating cells, defined as small regions of high reflectivity from which a trail of hydrometeors originates (American Meteorological Society 2023), at cloud top have been observed by radar for many decades. Early studies of generating cells often used vertically pointing radar to detect these kilometer-scale features (e.g., Marshall 1953; Wexler and Atlas 1959; Carbone and Bohne 1975). These studies documented that generating cells were favorable locations for ice to form and fall out leading to the trails observed on radar, and that these cells may be the result of convective instability possibly due to the advection of

Corresponding author: Sarah A. Tessendorf, saraht@ucar.edu

DOI: 10.1175/JAS-D-23-0029.1

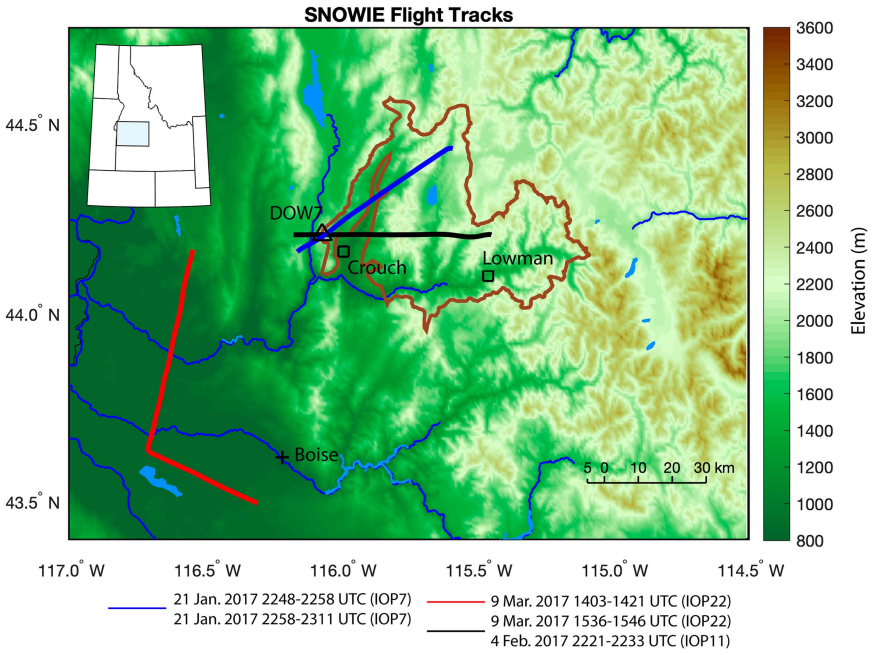

FIG. 1. Map of the observational domain for SNOWIE in western Idaho. UWKA flight segments analyzed for the 21 Jan 2017 case (IOP7) are shown as a blue line. The black line is the west–east-oriented flight legs from the 4 Feb (IOP11) and 9 Mar 2017 (IOP22) cases, and the red line represents the ascent leg heading northwest and then north from the 9 Mar 2017 (IOP22) case. The Payette basin is outlined in brown, which was the focal area for SNOWIE research flights. Rawinsondes analyzed for these cases were launched from Crouch and Lowman, Idaho, (squares). The location of the Doppler-on-Wheels radar (DOW7) is also shown (triangle).

dry air above the generating cell level. Hobbs et al. (1980) and Houze et al. (1981) calculated that cloud-top generating cells in an extratropical cyclone contributed to ~20%–35% of precipitation mass that reached the ground, while the rest accumulated through the conversion of cloud water as the ice particles fell through the cloud. Evans et al. (2005) and Ikeda et al. (2007) documented generating cells using S-band radar data in the Pacific Northwest, and Kumjian et al. (2014) used X-band radar to study them along the Colorado Front Range. From the data available in these studies, they documented the presence of supercooled liquid water in the generating cells, as well as enhanced ice concentrations, suggesting strong vertical motions are likely present in these cells.

Modern-day high-resolution airborne cloud radars have detected generating cells in many regions of the world, from the continental United States to the Arctic to the Southern Ocean (McFarquhar et al. 2011; Plummer et al. 2014; Rauber et al. 2014; Rosenow et al. 2014; Plummer et al. 2015; Rauber et al. 2015, 2017; Wang et al. 2020). These studies have shown that some generating cells are subkilometer in scale. At this scale, they will often be unresolved by present-day operational numerical weather prediction models. These modern-day studies have also utilized airborne sensors to characterize the in situ measurements in generating cells. Plummer et al. (2014, 2015) showed that the vertical motions within generating cells promote ice nucleation and growth in midlatitude cyclones. Similar findings were reported in generating cells observed over the Southern Ocean by Wang et al. (2020). In winter orographic clouds, studies by Ikeda et al. (2007) and Kumjian et al. (2014) came to similar conclusions about generating cells promoting ice growth, although the resolution of the scanning radar measurements from those studies rendered their focus on kilometer-scale generating cells compared to the sub-kilometer-scale cells that have now been observed with high-resolution airborne cloud radars. Therefore, the in situ characteristics of sub-kilometer-scale generating cells in orographic clouds have yet to be carefully examined and documented.

During the Seeded and Natural Orographic Wintertime clouds: the Idaho Experiment (SNOWIE) field campaign (Tessendorf et al. 2019), high-resolution airborne cloud radar measurements demonstrated that sub-kilometer-scale generating cells are fairly ubiquitous in winter orographic clouds. This study utilizes the high-resolution, airborne cloud radar and in situ measurements from SNOWIE to examine the microphysical conditions inside and outside of cloud-top generating cells observed in winter orographic clouds. While generating cells were frequently observed during SNOWIE, this study focuses on the three research flights that flew through the tops of generating cells providing the in situ measurements needed for this analysis.

The focus of this paper is to document characteristics of generating cells in winter orographic clouds using modern-day instrumentation. Section 2 describes the data and methods used in the analysis. Sections 3–5 provide an overview of each case

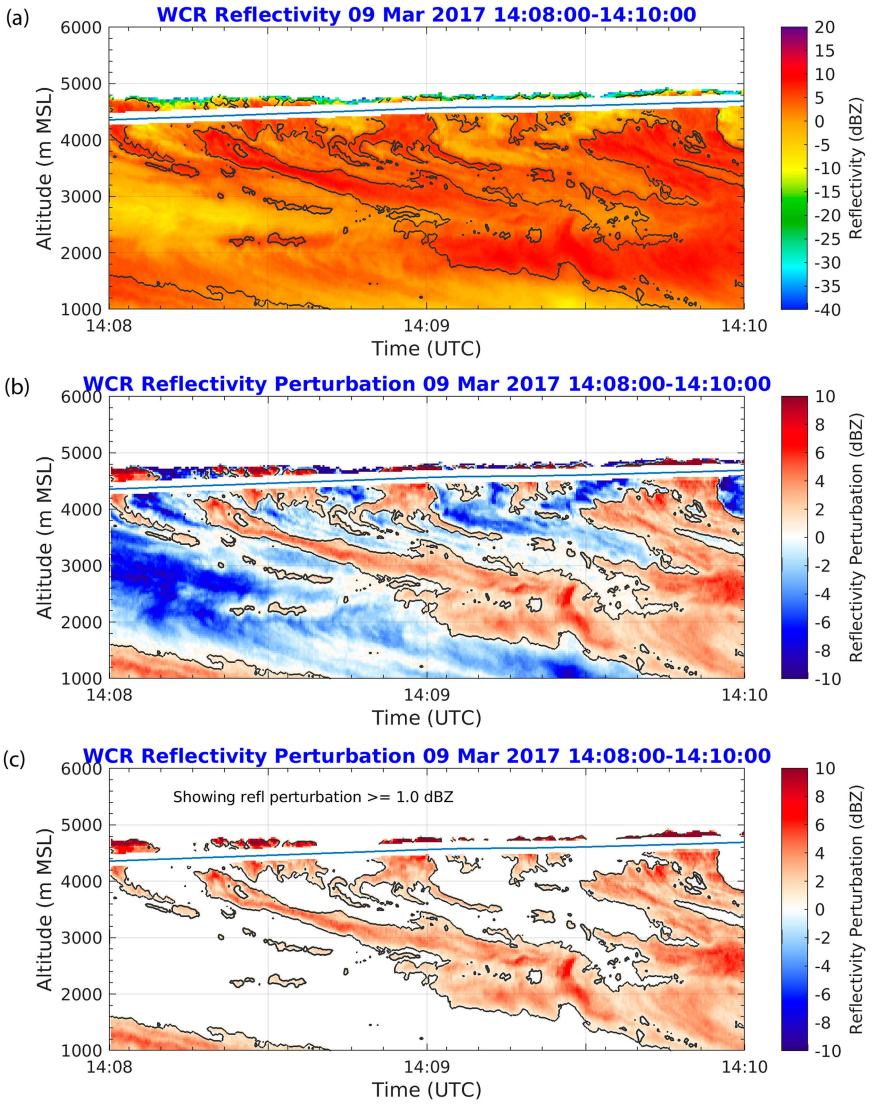

FIG. 2. (a) WCR reflectivity, (b) perturbation reflectivity, and (c) perturbation reflectivity $> +1$ dBZ for the 1408–1410 UTC segment on 9 Mar 2017 (IOP22). In all panels, the $+1$-dBZ reflectivity perturbation is highlighted in black solid contours. For the broader context of this flight segment, see Fig. 8.

with in situ measurements in cloud-top generating cells and examines the detailed microphysical conditions inside and outside generating cells from selected flight segments. Section 6 presents a summary of the microphysical conditions in generating cells from all flight segments through cloud-top generating cells during these three cases. A discussion and summary are provided in sections 7 and 8, respectively.

2. Data and methods

The data utilized in this study were collected during the SNOWIE field campaign in the winter of 2017, as described in Tessendorf et al. (2019). The University of Wyoming King Air (UWKA) was equipped with instruments measuring in situ microphysical data in clouds at a temporal resolution of 25 Hz and with the W-band Wyoming Cloud Radar (WCR; Wang et al. 2012), which collected vertical profiles of reflectivity and Doppler velocity above and below the aircraft position.[1] A complete list of instruments on the UWKA during SNOWIE are listed in Tessendorf et al. (2019). Those most relevant to this study include the Nevzorov probe (Korolev et al. 2013) to measure bulk cloud water and ice mass; the Cloud Droplet Probe (CDP; Lance et al. 2010; Faber et al. 2018) to measure cloud droplet size distribution and number concentration;

[1] As documented in Wang et al. (2012), the first usable range gate is ~100 m from the aircraft. This results in a gap in radar data about the flight-level altitude.

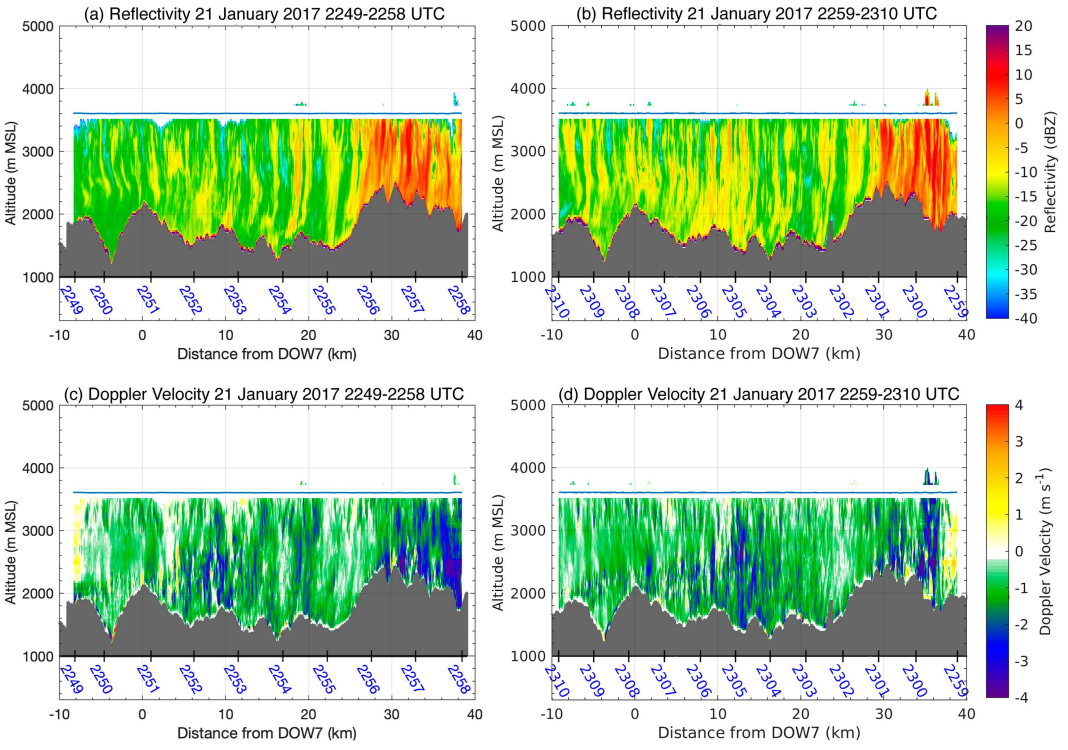

FIG. 3. (a),(b) WCR reflectivity and (c),(d) Doppler vertical velocity along two UWKA flight legs on 21 Jan 2017 (IOP7) (see Fig. 1, blue line). (a),(c) The flight leg between 2249 and 2258 UTC is the northeast heading leg, and (b),(d) the flight leg from 2259 to 2310 UTC is the southwest heading leg. Time (UTC) of the flight location is indicated in blue text along the x axis. Also, the x axis shows distance from DOW7, which was located atop Packer John mountain at $x = 0$ km. All research flight legs were anchored about this point during the SNOWIE campaign.

and the two-dimensional stereo optical array probe (2D-S; Lawson et al. 2006) that measures the particle habits and the size distribution of particles >50 μm. In addition, a Rosemount icing probe provided a measure of when supercooled liquid water was present and a five-hole gust probe provided in situ measurements of vertical air motion.

The 2D-S data used in this study were processed as described in Table 1 of Tessendorf et al. (2021) following methods by Korolev and Field (2015) and references therein. This analysis focused on 2D-S particles > 100 μm in order to infer particle type and phase based on the assumption that liquid droplets produce circular images, whereas ice particles have noncircular images, and the data processing was performed in two stages. During the first stage, the processing software extracted properties of all image frames and all individual images inside the image frames, which included interarrival times, number of images per frame, various image sizes, areas, perimeters, hollowness, roundness, etc. During the second stage, the processing software performed a sequence of procedures to determine acceptance and rejection of particle images, aiming to filter out various image artifacts. These artifacts can be caused by ice shattering, diffraction effects, electronic noise, optics contamination, and liquid shedding. Finally, separate size distributions were calculated for the accepted liquid (i.e., drizzle) droplets and ice particles for each averaging (1-s) time interval. More details on the specific steps to process the 2D-S data are outlined in Tessendorf et al. (2021).

In addition to the UWKA data, rawinsondes were released regularly from three sites within the observational domain (Fig. 1), providing thermodynamic profile data every 2–3 h for each SNOWIE research flight. Given the mixed-phase nature of these clouds, some sounding profiles exhibited superadiabatic profiles at cloud top due to presumed wet-bulbing effects (Ciesielski et al. 2012) and were therefore not included in this analysis where possible.[2] SNOWIE data, as well as synoptic weather maps and radar and satellite imagery from during the field campaign, are available via the online Field Catalog[3] managed by NCAR's Earth Observing Laboratory (EOL).

Objective identification of generating cells

The goal of this study is to examine the microphysical characteristics of generating cells. To do this in an objective way, we applied a method to identify the generating cells in the WCR radar reflectivity field, from which we determined the times that the UWKA in situ measurements were collected inside and

[2] The sounding data for IOP7 on 21 January 2017 may still have wet-bulbing effects, but there was no other sounding time that was representative of this IOP flight.

[3] http://catalog.eol.ucar.edu/snowie.

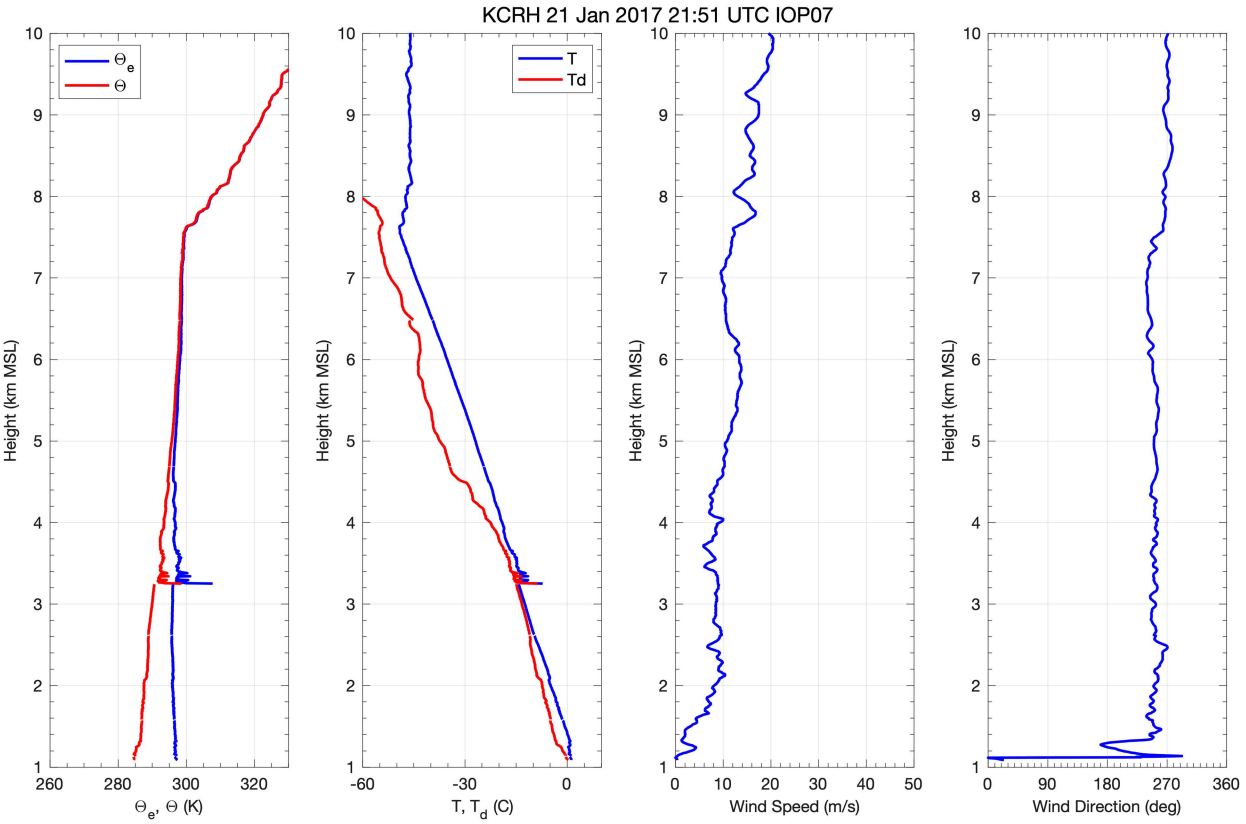

FIG. 4. Vertical profiles of thermodynamic variables from the atmospheric sounding launched at Crouch at 2151 UTC 21 Jan 2017 (IOP7). (left to right) Potential temperature (θ; K; red) and equivalent potential temperature (θ_e; K; blue), temperature (°C; blue) and dewpoint temperature (°C; red), wind speed (m s^{-1}; blue), and wind direction (°; blue), respectively.

outside the generating cells. Previous studies have used reflectivity local maxima or prominence >4 dB and then either a constant time interval surrounding the peak or a dBZ threshold relative to the peak to define data within the generating cell (Plummer et al. 2014; Wang et al. 2020). In Wang et al. (2020) they went a step further to also require rising motion in the generating cells; however, we chose not to include vertical velocity as a criterion in how we identified generating cells in order to characterize the vertical velocity characteristics of the cells.

The method we applied to objectively identify generating cells was based upon identifying perturbations in the radar reflectivity field. The perturbation reflectivity was computed by calculating the average WCR reflectivity over a particular flight segment at each vertical level of the upward- and downward-looking radar beams, which has a gate spacing of roughly 30 m. Flight segments were identified based upon observed reflectivity structures, with the goal of having similar structures contained in a given segment. To maintain consistency in the application of this method, segments were generally defined to be on the order of 2 min ± 30 s long.[4] Then, for each vertical level, the average reflectivity at the given level was subtracted from the reflectivity measurements at all gates at that vertical level to determine the perturbation from the average. Figure 2 illustrates an example of how the perturbation reflectivity field delineates the generating cells regions near cloud top from the 9 March 2017 case, especially in areas with greater than 1-dBZ perturbation.

The WCR perturbation reflectivity closest to the aircraft was determined in all cases presented herein from the downward-looking WCR beams.[5] Typically, the distance to the first measurable gate is about 90–120 m (3 gates or 4 gates × 30-m gate spacing) away from the aircraft. If there were no detectable cloud/precipitation targets within 180 m of the aircraft, it means that the aircraft was outside of cloud/precipitation.[6] Finally, the

[4] The segment beginning at 2227:00 UTC 4 February 2017 is the exception as it was 6 min long because the cloud structure was very consistent across this longer segment.

[5] We also examined reflectivity patterns using radar data from the upward-looking WCR beams; however, in the cases presented herein the aircraft was flying at or near cloud top, so the downward-looking beam captured the generating cells best, as there was often negligible reflectivity data above the aircraft.

[6] Specifically, the minimum detectable reflectivity (provided in the WCR data files) was used to filter if reflectivity was measured, which generally was −40 ± 0.5 dBZ. If no radar echo greater than this minimum detectable reflectivity was present from the upward-looking beam at a particular sample time within the vertical distance of 180 m, then WCR/UWKA is out of cloud or just at the very top.

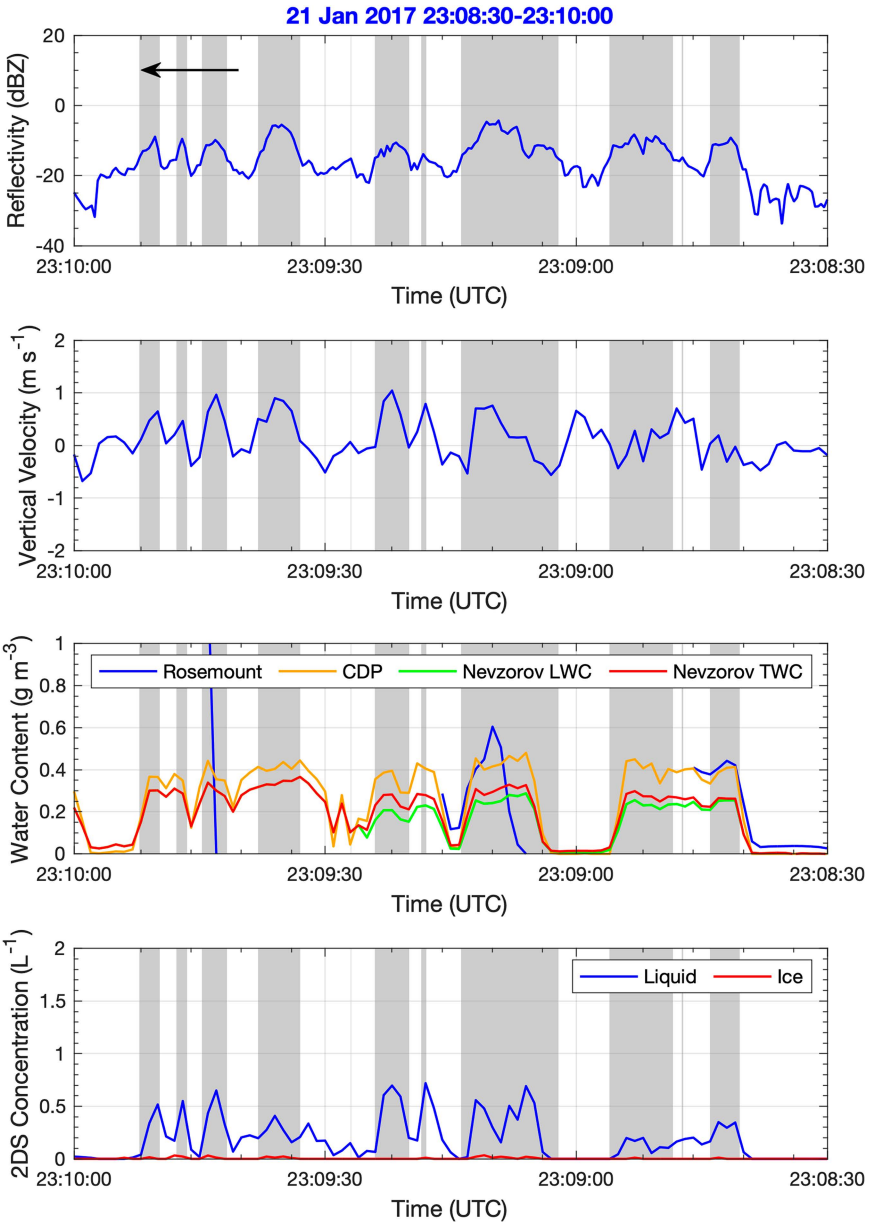

FIG. 5. Time series traces of UWKA measurements during the 2308:30–2310:00 UTC segment on 21 Jan 2017 (IOP7). (top to bottom) The WCR reflectivity (dBZ) at the nearest radar gate below the UWKA aircraft flight level, the observed vertical velocity (m s^{-1}) measured by the gust probe at the UWKA aircraft flight level, the measured water content (g m^{-3}) from the Rosemount, Nevzorov, and DMT CDP probes on the UWKA (see legend), and the total liquid (blue) and total ice (red) concentration (L^{-1}) for particles > 100 μm as measured by the 2D-S optical array probe. The gray shading denotes times within generating cells.

WCR reflectivity perturbation closest to the aircraft body, which is sampled at a rate of 3–4 Hz, was interpolated to the time of UWKA's 25-Hz flight-level data. The reflectivity perturbation threshold of 1 dBZ was used to determine the times when the UWKA instrument measurements were collected inside ($\geq$1 dBZ perturbation) and outside ($<$1 dBZ perturbation) of generating cells, in order to identify the in situ measurement characteristics of generating cells. We examined the sensitivity of identifying the generating cells by a manual identification process versus using various thresholds of perturbation reflectivity and determined that the threshold of $>+1$ dBZ was the most appropriate to objectively identify generating cells for subsequent analysis.

Three cases from SNOWIE were selected for this analysis based upon the presence of cloud-top generating cells in the WCR reflectivity data, and for which in situ measurements were collected in the generating cells within 500 m of cloud top.

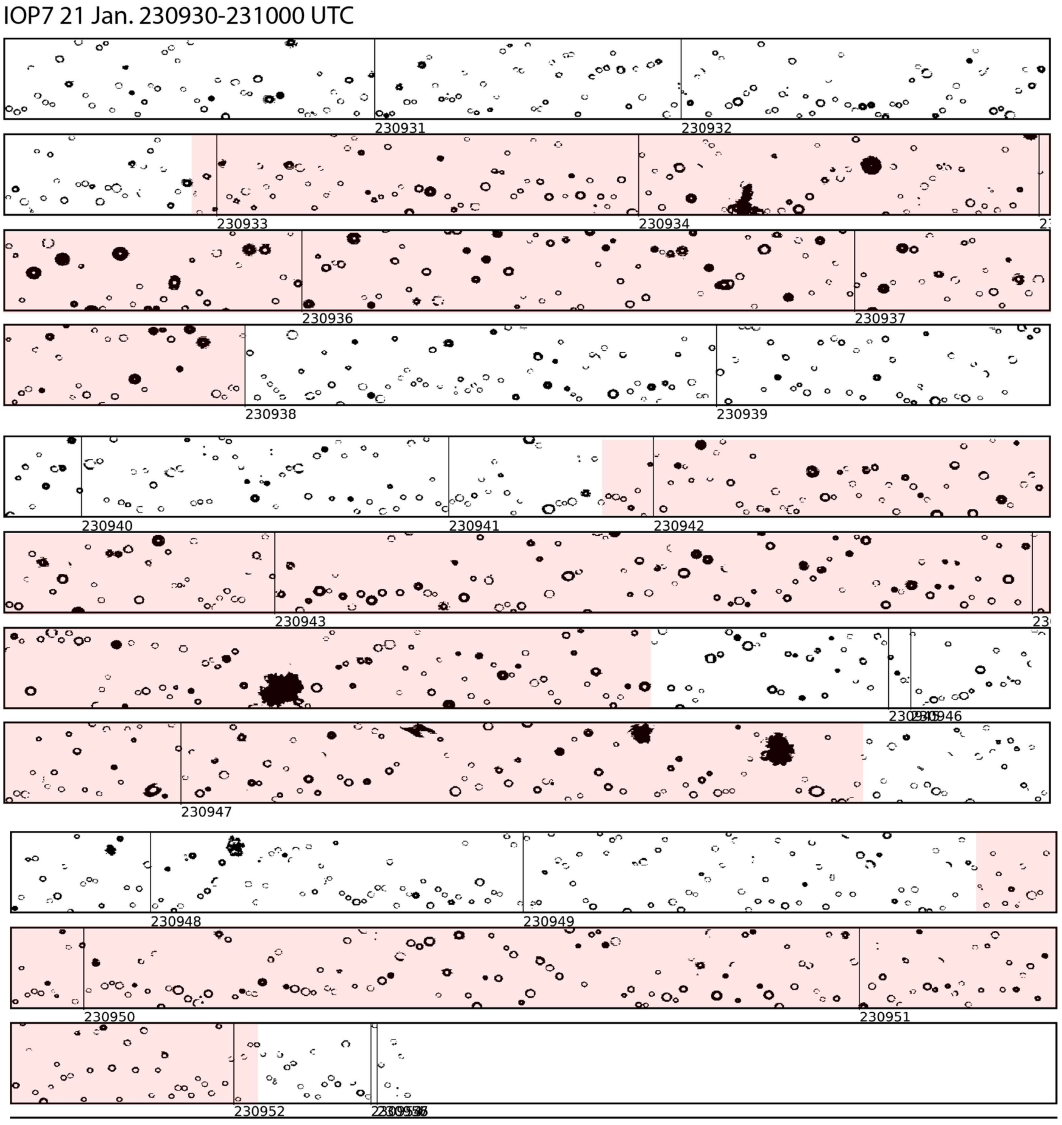

FIG. 6. 2D-S images of all particles > 100 μm between 2309:30 and 2310:00 UTC 21 Jan 2017 (IOP7). The red shading indicates times when the aircraft was inside generating cells. The buffer window height of each panel is 1.6 mm. Note that there were no particles measured >100 μm between 2309:53 and 2310:00 UTC (therefore, the times outside of generating cells in this segment are not adequately shown in this figure).

3. 21 January 2017 (IOP7)

The synoptic pattern on this day was characterized by a 500 hPa trough off of the West Coast with southwesterly flow impacting Idaho (see Fig. 9 of Tessendorf et al. 2019). The IOP exhibited shallow orographic clouds that occurred after the passage of deep clouds associated with an atmospheric river. Generating cells were observed on 21 January 2017 at the top of the shallow orographic cloud (Fig. 3). A thin and localized cloud was present between 6 and 7 km MSL in a short (<10 km) segment above the orographic cloud; otherwise, no upper-level clouds were observed above the cloud-top generating cells (not shown). There was no evidence of ice particles falling into the generating cells at cloud top from an upper-level cloud, so all ice observed in the tops of these clouds were nucleated in situ. Cloud-top heights in this case were generally 3.6 km, with a few turrets reaching 3.8 km, and the UWKA flew at a constant altitude (3.6 km) through the tops of the cloud at a temperature of −16°C, which provided a sample of conditions in the tops of multiple generating cells that can be analyzed statistically. Reflectivity values in the cloud-top generating cells ranged between −8 and 16 dBZ, with fall streaks observed below the generating cells that extended to the surface and the highest reflectivity in cells over the highest terrain (Fig. 3). There was no visible bright band in the reflectivity of this cloud, given that the entire cloud layer was subfreezing (Fig. 4). The cloud top at 3.6 km was marked by a slight instability of no more than 200 m in depth; otherwise, the cloudy

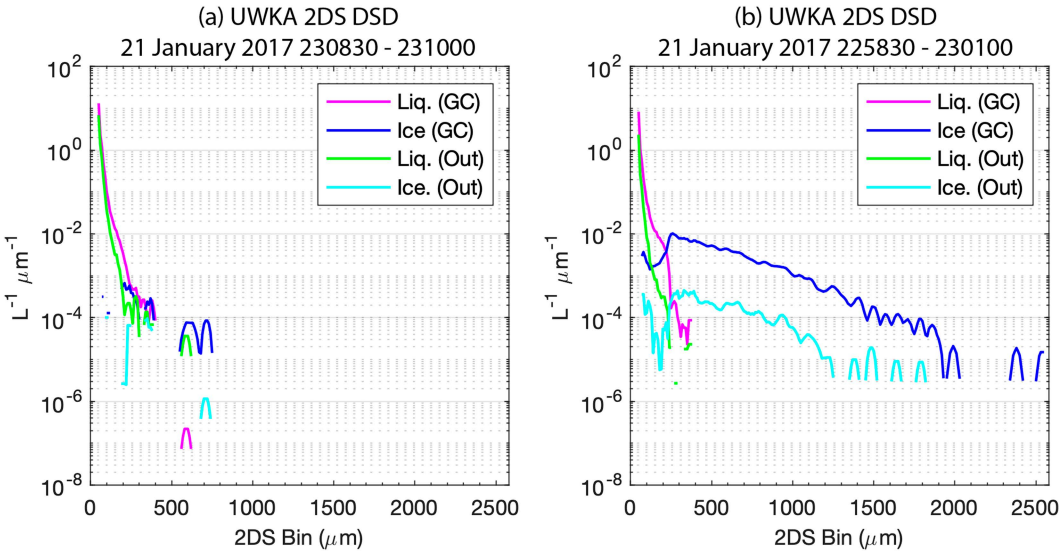

FIG. 7. Particle size distributions of 2D-S data in the (a) 90-s segment between 2308:30 and 2310:00 UTC and (b) a higher-reflectivity segment between 2258:30 and 2301:00 UTC shown in Fig. 3b on 21 Jan 2017 (IOP7). Magenta (liquid particles) and blue (ice particles) lines are measurements inside generating cells, while green (liquid particles) and cyan (ice particles) lines are from measurements outside generating cells.

layer of the atmosphere below 3.6 km was conditionally unstable (Fig. 4). Wind speeds throughout the cloud depth were <10 m s^{-1}, with nearly zero vertical shear (Fig. 4). Winds in this case were west-southwesterly throughout much of the troposphere above 1.5 km. During this IOP, the UWKA flew along the west-southwesterly wind for five flight legs at varying altitudes, and then perpendicular to the wind for the remaining flight legs. This analysis focuses only on the two flight legs flown parallel to the wind vector between 2249 and 2310 UTC[7] (blue line in Fig. 1).

Detailed microphysics measurements in IOP7

All of the flight legs shown in Fig. 3 provide in situ measurements in the tops of cloud-top generating cells. To illustrate the characteristics in these cells, we examine a 90-s segment between 2308:30 and 2310:00 UTC 21 January 2017 (Fig. 5). During this short segment, the UWKA flew through 11 generating cells using $>+1$ dBZ perturbation reflectivity below the aircraft flight level. The horizontal scale of these generating cells ranges from <33 m to 1 km based upon the time scales of the aircraft measurements given a mean aircraft speed of 98.9 m s^{-1}. Nine of these 11 generating cells are visible in Fig. 5 as gray shading, based upon the WCR reflectivity at the first valid gate below the flight level. In these 9 generating cells, a marked increase in liquid water content (LWC) and ice water content is also apparent (Fig. 5). These 9 cells had increases in both liquid and ice particles >100 μm in the in situ 2D-S measurements and indicate that these generating cells were characterized by having drizzle (liquid drops >100 μm) coexisting with some ice (see examples in Fig. 6). In fact, these cells had higher concentrations of drizzle than ice based on the images; however, when ice was observed it was inside only generating cells. Most of these generating cells were composed of upward vertical air motions on the order of 0.5–1 m s^{-1}, though some had a combination of upward and downward motions within them (Fig. 5). Generally, the generating cells had stronger vertical motions than the portions of the segment surrounding each cell.

The particle size distribution (PSD) observed by the 2D-S in this 90-s segment (maximum reflectivity of -5 dBZ) shows that the liquid and ice particle distributions inside generating cells have a higher concentration of particles in the 200–300-μm size range, as well as a few occasional ice particles larger than 500 μm (Fig. 7a). These trends are even more apparent when comparing the PSDs from a higher reflectivity segment (10–15 dBZ) through cloud top (Fig. 7b). Here, the enhancement in drizzle inside generating cells is clearly distinguished from the liquid particle PSD outside of generating cells, and the PSD of ice particles is more complete and shows ice in much higher concentrations at all sizes. These observations indicate that drizzle was readily forming in this cloud, and ice formation was limited to within the generating cells, and was especially active in the higher reflectivity segments which coincided with the highest terrain.

4. 9 March 2017 (IOP22)

The synoptic pattern on this day was characterized with a 500 hPa trough embedded in northwest flow (see Fig. 9 from Tessendorf et al. 2019). The earliest flight segment on 9 March, which occurred during the ascent of the UWKA aircraft out of Boise airport over the Snake River valley (see red track in

[7] Cloud seeding was conducted on this case using ground-based generators beginning at 2230 UTC; however, model simulations and stable atmospheric conditions do not suggest that cloud seeding materials impacted the cloud-top measurements.

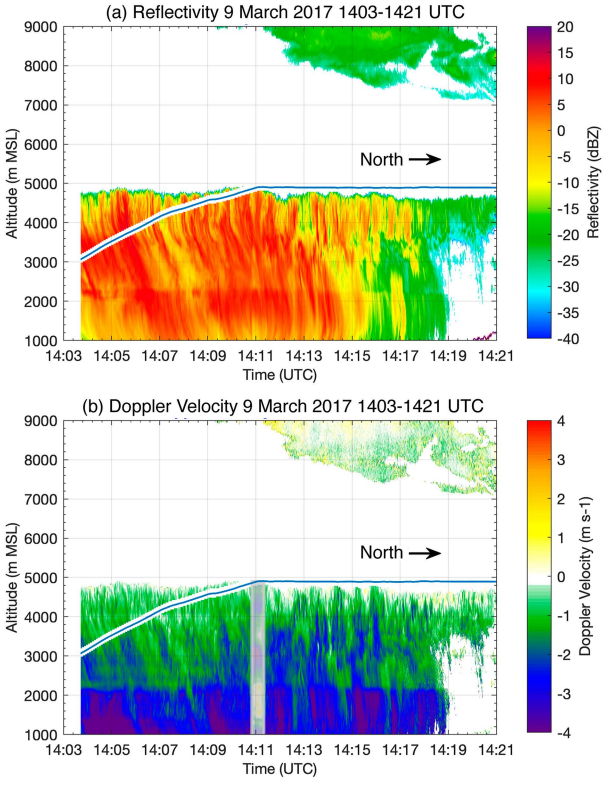

FIG. 8. (a) WCR reflectivity and (b) Doppler vertical velocity along the beginning of the IOP22 UWKA flight from 1403 to 1421 UTC 9 Mar 2017 (Fig. 1, red line). Note that the aircraft heading changed at 1411 UTC leading to the anomaly in the WCR data, especially noticeable in the vertical velocity measurements (gray shaded area), due to the aircraft not flying straight and level during the turn. These data are plotted along a time axis as opposed to distance, since the aircraft was not yet in a position to fly set flight legs over the terrain at this time.

Fig. 1), shows a low-level cloud with a top of approximately 4800–4900 m (Fig. 8) and temperature of −15°C. Along the cloud top, generating cells were present with reflectivity > 5 dBZ. The generating cells had enhanced reflectivity fall streaks below them. A bright band was detected in the reflectivity field around 2200 m, with increased fall speeds in the Doppler velocity data from particles melting at this level. The segment between 1408 and 1410 UTC exemplified the reflectivity perturbation methodology (Fig. 2) and will be inspected more closely as the aircraft flew through the generating cells within 500 m of the cloud top (in the next section). At the time and location where the aircraft flew through the cloud top, only a single cloud layer was present; however, after 1411 UTC, when the UWKA aircraft turned north toward the intended research flight track over the Payette basin, an upper cloud was observed on the radar. Initially, this upper cloud was confined altitudes above 8000 m, but as the UWKA aircraft approached the intended flight track at the end of this flight segment, the upper cloud lowered to between 7000 and 8000 m (Fig. 8).

Later in the flight, when the research flight tracks were over the Payette basin (black line in Fig. 1), the WCR-observed cloud structure was composed of two cloud layers: an upper layer between ~5500 and 8000 m and a lower layer between the surface and ~4600–4800 m (Fig. 9a) with a lower cloud-top temperature of −15°C. The upper cloud base lowered slightly throughout the flight (Fig. 9b), such that its base was <500 m above the lower echo top. There was no reflectivity detected above the minimum unambiguous signal level (−40 dBZ) in the intervening dry layer, indicating that it was very unlikely that hydrometeors were falling from the upper cloud and into the lower cloud. There was no cloud seeding conducted in this IOP.

The lower cloud was composed of multiple vertically oriented generating cells near cloud top, with associated particle fall streaks below them. Reflectivity in the generating cells in the flight segment between 1536 and 1546 UTC reached −5 dBZ (Fig. 9a) and strengthened over time to 5 dBZ by 1616–1623 UTC (Fig. 9b). The fall streaks from the generating cells in the 1538–1546 UTC flight leg did not always reach the surface with the same values of reflectivity observed at cloud top; however, by the later flight leg of 1616–1623 UTC the reflectivity values in the generating cells at cloud top extended to the surface. The vertical wind shear in this case makes tracing the fall streaks within the plane that the WCR observes more challenging, compared to that on 21 January 2017 (IOP7; Fig. 3). The flow over the underlying terrain is visible in the Doppler velocity field as broad vertical velocity undulations associated with regions with the highest terrain (as shown in Zaremba et al. 2022), evident in both the upper and lower cloud layers. A noticeable bright band is apparent in both the reflectivity and Doppler velocity fields in these flight legs.

During this and later flight legs, the aircraft flew a porpoise maneuver to profile the tops of the lower cloud layer while avoiding excessive ice accumulation on the aircraft by not residing in regions with high SLW near cloud top for prolonged periods of time. There are two segments within the flight leg illustrated in Fig. 9a where the aircraft flew within 500 m of cloud top through generating cells. These segments will be examined more thoroughly in section 4a.

The atmosphere for this case was generally stable and/or well mixed from the surface to 2800 m from the θ_e profile. Between 2800 and 3300 m, a layer of potential instability existed (Fig. 10), which corresponded to the altitude where embedded convective elements were observed in the reflectivity 20–28 km east of DOW7 (Fig. 9). Above this, the atmosphere was stable again through 4800 m, which corresponded with the lower cloud top in this profile and where there were cloud-top generating cells observed. A second potential instability layer existed between 4800 and 5300 m (Fig. 10). Above 5300 m, the atmosphere was stable. The sounding in Fig. 10 shows southwesterly winds between 1500 and 2200 m veering to westerly by 2500 m and west-northwesterly above 3500 m. Wind speeds increased throughout the profile, except for a layer of constant wind speed between 2800 and 3300 m and a layer with nearly constant, but decreasing, speeds between 4800 and 5300 m. These two layers of nearly constant wind speeds correspond to the two layers of potential instability.

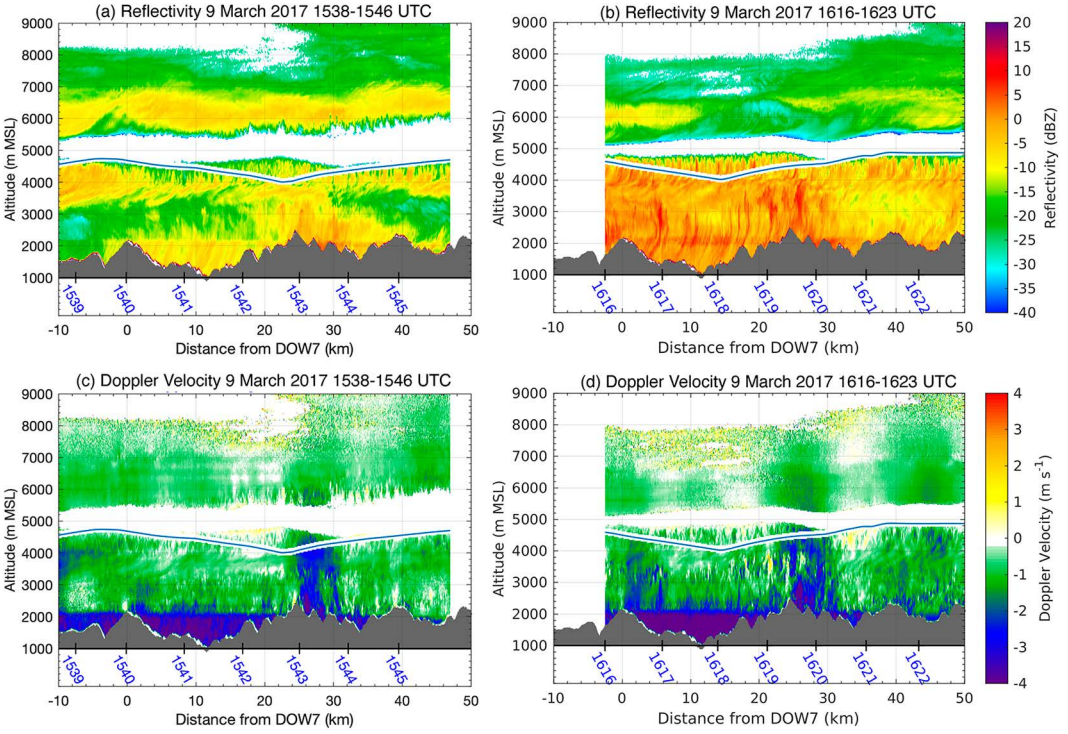

FIG. 9. (a),(b) WCR reflectivity and (c),(d) Doppler vertical velocity along UWKA flight leg (a),(c) from 1538 to 1546 UTC and (b),(d) from 1616 to 1623 UTC 9 Mar 2017 in IOP22 (black line in Fig. 1). Time (UTC) of the flight location is indicated in blue text along the x axis. Also, the x axis shows distance from DOW7, which was located atop Packer John mountain at $x = 0$ km. All research flight legs were anchored about this point during the SNOWIE campaign.

Detailed microphysics measurements in IOP22

The 1408–1410 UTC segment (hereafter segment IOP22A) on 9 March 2017 (previously shown in Fig. 2) indicated the UWKA aircraft flew through 14 generating cells using >1 dBZ perturbation reflectivity above the aircraft flight level; however, several of those are very short periods (~1 s or less) given they just barely reached the +1 dBZ threshold (Fig. 11). The widths of these cells ranged from <33 m to over 900 m. Seven of the 14 identified generating cells were on a horizontal scale of roughly 200 m or longer given a mean aircraft speed of 98.9 m s^{-1}, while the rest are less than 200 m in width at the location the aircraft flew through. It is likely that the more spurious generating cells may have been sampled on the horizontal periphery and not in the central core of the cell. The seven broader (>200-m width) generating cells are visible in Fig. 11, based upon the WCR reflectivity perturbation a gate below the flight level and can also be visualized in Fig. 2.

In these seven generating cells, a marked increase of at least 0.25 m s^{-1} in vertical velocity is noted, except for the cell from 1409:22 to 1409:26 UTC (hereafter "outlier" generating cell), and correspondingly there is also an increase in total water content in these cells of at least 0.1 g m^{-3} with peaks of 0.2 g m^{-3} (Fig. 11), although less so for the "outlier" cell. Most of the total water content measured by the Nevzorov in these cells was ice, as the cloud water content in these cells was <0.05 g m^{-3}. In all of these seven generating cells, drizzle drops coexisted with ice (see examples in Fig. 12), albeit the drizzle concentration was less in the "outlier" cell. Ice >100 μm and drizzle concentrations in these generating cells were on the order of 1 L^{-1} or greater (Fig. 11). The habits of the ice particles were platelike, including dendrites and stellar crystals, with occasional plate-capped columns, which suggest they were formed by primary ice nucleation. Outside of the generating cells, there were periods of 2D-S data with low concentrations of both ice and liquid, such as between 1409:33 and 1409:39 UTC, that consisted of just a few ice crystals >100 μm (Fig. 12), and then there were periods where the 2D-S ice concentration >100 μm was on the order of 0.5 L^{-1} while the liquid (drizzle) concentration was still low. The 2D-S measurements of particles >100 μm in the interim segments outside the 14 generating cells consisted of fewer particles overall (liquid and ice) compared to the segments inside generating cells (Fig. 11).

In the flight segment between 1544 and 1545 UTC (hereafter IOP22B), during a time when the UWKA flew over the mountains of the Payette basin and an overlying cloud was present, generating cells were observed at the top of the lower-level cloud and reflectivity values were generally 10–15 dBZ less than in the IOP22A segment (Fig. 11). During this segment, the aircraft was in the ascending portion of its porpoise maneuver, and within 200 m of cloud top, which is when the generating cells were most apparent in the WCR reflectivity. During this 60-s

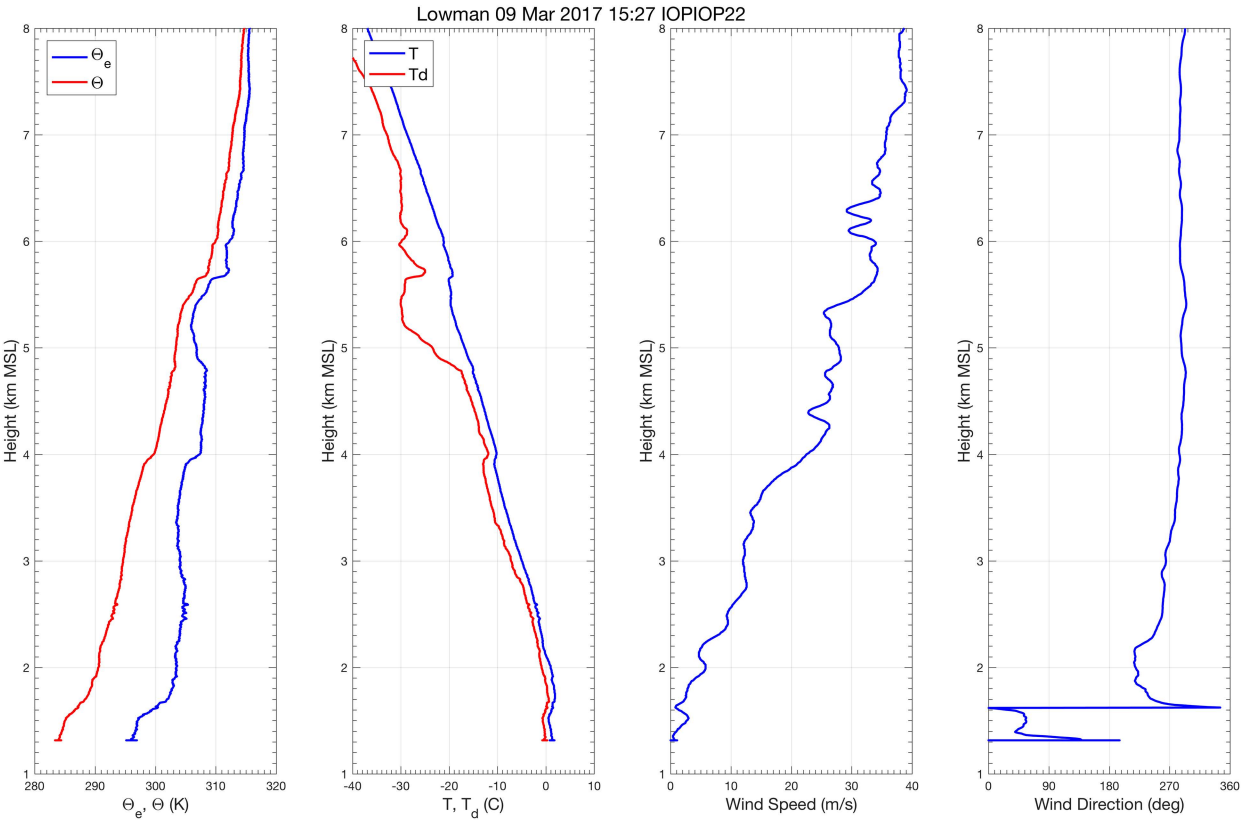

FIG. 10. Vertical profiles of thermodynamic variables from the atmospheric sounding launched at Lowman at 1527 UTC 9 Mar 2017 (IOP22). (left to right) Potential temperature (θ; K; red) and equivalent potential temperature (θ_e; K; blue), temperature (°C; blue) and dewpoint temperature (°C; red), wind speed (m s^{-1}; blue), and wind direction (°; blue), respectively.

segment, 15 generating cells were detected based upon the >+1 dBZ perturbation reflectivity threshold using the reflectivity a gate below the aircraft (Fig. 11). The widths of these generating cells was between 50 and 700 m, with seven being greater than 200 m in length. The vertical air motions in this 60-s segment were generally upward, in a region of orographically forced upward vertical motion (Fig. 9c), and >0.25 m s^{-1} stronger within the generating cells. The maximum LWC observed in the generating cells increased from 0.15 to 0.25 g m^{-3} as the aircraft approached the top of the cloud at the end of this segment (Fig. 11). Embedded within that overall increase in LWC with height are some smaller fluctuations in LWC, several of which are associated with the generating cells. More clearly visible are the reductions in LWC associated with the intervening regions between generating cells, especially in the first half of the segment before the aircraft got close to the cloud top. The two-dimensional stereo optical array probe particle concentrations >100 μm increase within each generating cell, albeit a factor of 10 lower than in the IOP22A segment (Fig. 11), which explains the reduced reflectivity values. Ice habits of the few ice crystals observed in the generating cells were pristine and rimed dendrites (not shown).

The PSD in the IOP22A segment shows a broad distribution of ice observed both in and out of the generating cells, though there is a consistently higher concentration of ice of all sizes inside generating cells (Fig. 13a). There is an enhanced concentration of liquid (drizzle) particles between 100 and 400 μm in this segment within the generating cells. In the IOP22B segment, between 1544 and 1545 UTC, the concentration of ice particles inside the generating cells is greater than the regions outside of the generating cells, especially at sizes between 100 and 300 μm, but to a lesser degree than in Fig. 13a. Much less drizzle and ice overall was measured by the 2D-S in the IOP22B segment compared to the IOP22A segment. Rather, the IOP22B had more cloud water while IOP22A had very little (Fig. 11). The liquid PSDs inside and outside the generating cells of IOP22B show a slight enhancement of concentrations between 100 and 200 μm inside the generating cells. These observations indicate that drizzle was readily forming in IOP22A, in concert with active ice growth thereby depleting the cloud water in that segment. Whereas in IOP22B, drizzle had not formed in same magnitude of concentrations as IOP22A, and ice was also not forming or growing as actively, thereby more cloud water was still present.

5. 4 February 2017 (IOP11)

Similar to IOP22, the synoptic pattern on 4 February 2017 (IOP11) was characterized with a 500 hPa trough embedded in northwest flow (see Fig. 9 from Tessendorf et al. 2019). The

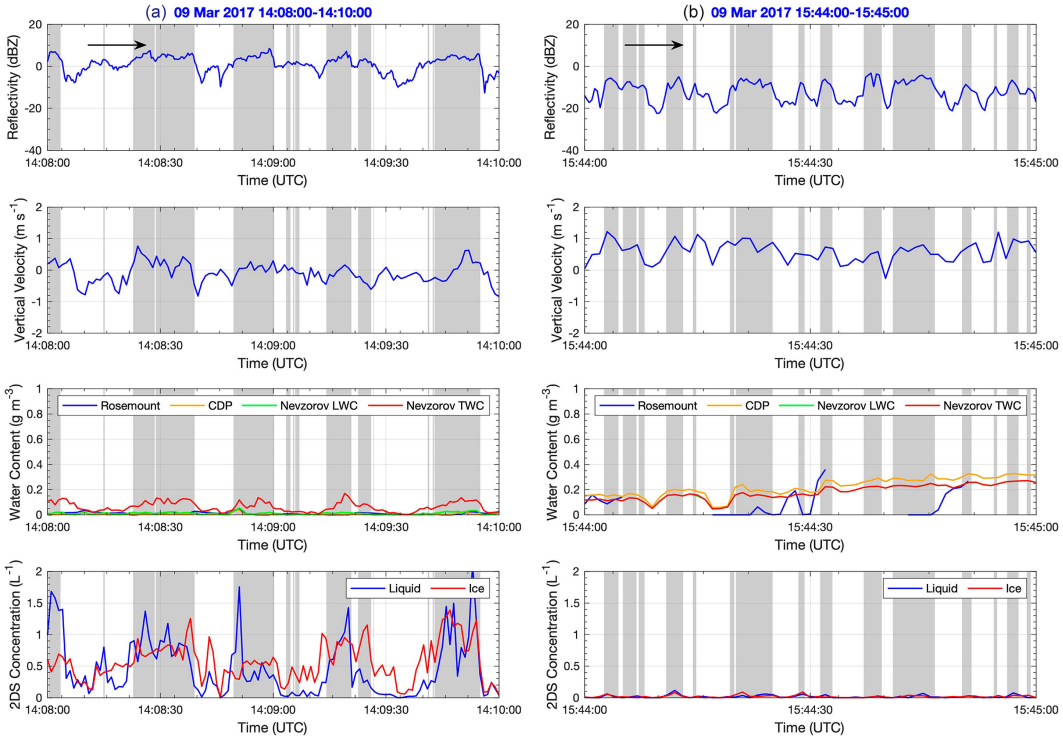

FIG. 11. Time series traces of UWKA measurements (a) during the 1408–1410 UTC segment (IOP22A) and (b) the 1544–1545 UTC segment (IOP22B) on 9 Mar 2017 (IOP22). (top to bottom) The WCR reflectivity (dBZ) at the nearest radar gate below the UWKA aircraft flight level, the observed vertical velocity (m s^{-1}) measured by the gust probe at the UWKA aircraft flight level, the measured water content (g m^{-3}) from the Rosemount, Nevzorov, and DMT CDP probes on the UWKA (see panel 3 legend), and the total liquid (blue) and total ice (red) concentration (L^{-1}) for particles >100 μm as measured by the 2D-S optical array probe. The gray shading denotes times within generating cells.

cloud structure on this day also shows multiple layered clouds, similar to IOP22 (Fig. 14). In this case, the lower cloud layer top height varied, generally extending up to 6200–6600 m, and exhibited cloud-top generating cells between 5800 and 6300 m MSL and this lower cloud top was much colder than in the previous two IOPs (−30°C). The upper cloud layer was detected between 7400 and 9500 m MSL. The bottom of the upper cloud layer in this case was ragged, similar to that in IOP22. There was no W-band reflectivity detected >−40 dBZ between the cloud layers, which suggests that there were no cloud particles falling from the upper to the lower layer. Within the lower cloud, the reflectivity structure was composed of fall streaks emanating from cloud-top generating cells with reflectivity values between 0 and 10 dBZ. There were also some isolated areas of apparent embedded convection with tops around 3500 and 4600 m, which corresponds with two shallow levels of potential instability shown in the sounding profile (Fig. 15) and also had associated fall streaks extending to the surface. The reflectivity in these features was greater than in the rest of the cloud, often >15 dBZ, and the Doppler velocity data in several of these indicated stronger negative velocities suggesting these cells contained larger and faster-falling particles, such as graupel (Fig. 14). A bright band was detected in this case around 1700 m MSL, near the altitude of the freezing level shown in the sounding (Fig. 15). This analysis focuses on when the UWKA flew through the tops of the generating cells, in flight legs between 2205 and 2233 UTC.[8]

The 2321 UTC sounding from Crouch, Idaho, on 4 February 2017 showed that the atmosphere was generally stable throughout the lower cloud layer, with some isolated layers of instability. The most notable instability was at the cloud-top altitude of 6500 m (Fig. 15). However, there were isolated and very shallow instabilities at 1900, 3500, and 4600 m (shallow decreases in θ_e). Above 4800 m, the profile was stable through the cloud top at 6500 m (−30°C) where the more notable, yet still shallow, instability was observed. Wind speeds veered and increased with height from the surface up to 2800 m. Above 2800 m, wind speeds were fairly constant and from the west-southwest. Wind speeds more than doubled from 4800 to 6200 m, while maintaining the general west-southwesterly direction, and then were approximately 36 m s^{-1} and westerly above that height.

[8] Ground-based seeding was conducted prior to 1920 UTC in this case, and airborne seeding began after 2255 UTC. There was no seeding conducting during this analysis period.

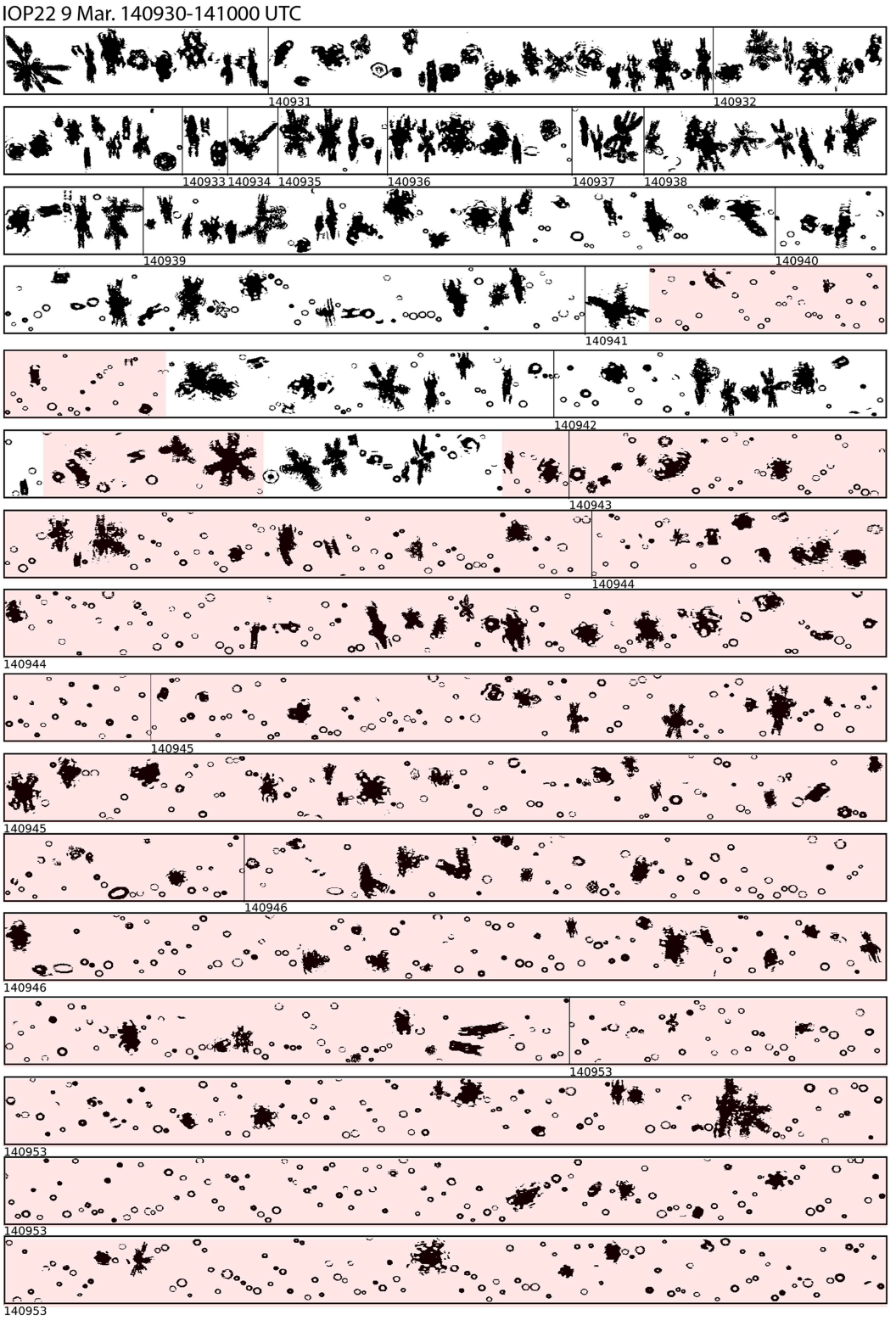

FIG. 12. 2D-S images of all particles >100 μm observed on 9 Mar 2017 (IOP22) between 1408:00 and 1409:48 UTC. The red shading indicates times when the aircraft was inside generating cells. The buffer window height of each panel is 1.6 mm.

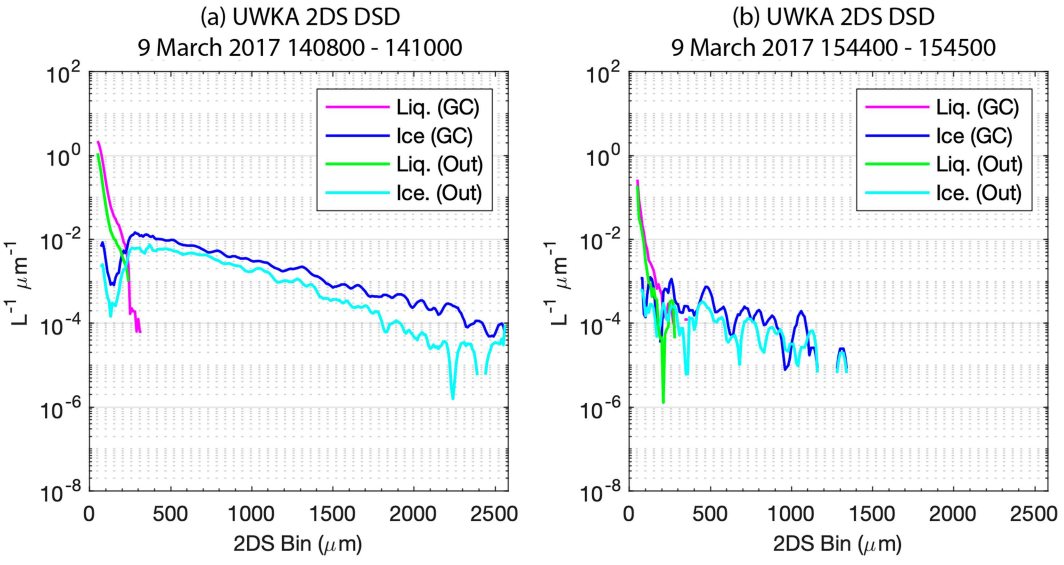

FIG. 13. Particle size distributions of 2D-S data in segments (a) between 1408 and 1410 UTC (IOP22A) and (b) between 1544 and 1545 UTC (IOP22B) 9 Mar 2017 (IOP22). Magenta (liquid particles) and blue (ice particles) lines are measurements inside generating cells, while green (liquid particles) and cyan (ice particles) lines are from measurements outside generating cells.

Detailed microphysics measurements in IOP11

The flight segment between 2220:30 and 2223:00 UTC 4 February 2017 exhibits 22 generating cells based upon the >+1 dBZ perturbation reflectivity threshold (Fig. 16). The horizontal width of flight measurements in these generating cells ranges between <33 and 1000 m. There are eight cells longer than 200 m in width that are readily visible in Fig. 16, though two are so close together, they appear as one broader cell (only separated for less than half a second at 2222:05 UTC). The vertical air motions within this segment are predominantly upward, as this segment was in a broad region of ascending air linked to the terrain as confirmed in the WCR radial velocity data (Fig. 14b), and the vertical velocities tend to be stronger inside the generating cells (Fig. 16). The LWC trace is relatively constant (~0.05 g m^{-3}), except for detectable reductions in the regions between the broader generating cells. The 2D-S ice concentrations are greater than the drizzle concentrations in this segment, by more than double in some cells, and they tend to be enhanced inside the generating cells.

The PSD during this segment shows consistently higher ice concentrations inside generating cells at all sizes, especially for sizes greater than 500 μm (Fig. 17). The ice particle images detected by the 2D-S were irregular and lacked distinctive habit features, likely because they were rimed (Fig. 18). Given the cloud-top temperature (−30°C) and water saturated environment (as determined by the LWC measured by the CDP, Nevzorov, and Rosemount probes), it is possible these ice crystals were side planes or mixed habit crystals (Magono and Lee 1966; Bailey and Hallett 2009). There is virtually no difference between the liquid PSD inside and outside generating cells in this segment, and there are very few drizzle drops in the generating cells in this segment.

6. Comparison of measurements in all generating cells

Here we compare the measurements inside and outside generating cells for all segments analyzed to demonstrate that the general trends illustrated in the selected segments highlighted above are robust, while also documenting the variability observed in the generating cells across these cases. We also examine the generating cell size and its relationship to the observed generating cell characteristics.

a. *Reflectivity*

The measurements inside and outside of the cloud-top generating cells in segments through the cloud tops in these three cases are quantified and compared by box-and-whisker plots for reflectivity in Fig. 19. There is a distinct difference in the distributions of reflectivity in the generating cells as expected, since the cells were defined having higher reflectivity compared to neighboring cloudy regions (Fig. 19). Segments had a 5–8-dBZ median difference between the generating cells and surrounding cloud, though some segments had >12 dBZ difference. The median reflectivity in the generating cells ranged from −15 dBZ to near 5 dBZ, whereas it ranged from −26 dBZ to near 0 dBZ outside the generating cells.

The boxplots in Fig. 19 are shown in order of the median generating cell 2D-S ice concentration (Fig. 22b) in each segment, with the greatest ice concentration shown on the left of the figure. The segment with the greatest median reflectivity inside generating cells (5 dBZ) was on 9 March 2017 starting at 1408:00 UTC (shown on the far left in Fig. 19), which also had the greatest median ice *and* drizzle concentration of all segments (Fig. 22). Meanwhile, it had some of the least LWC (Fig. 21), indicating the presence of a vigorous mixed-phased process where ice was effectively

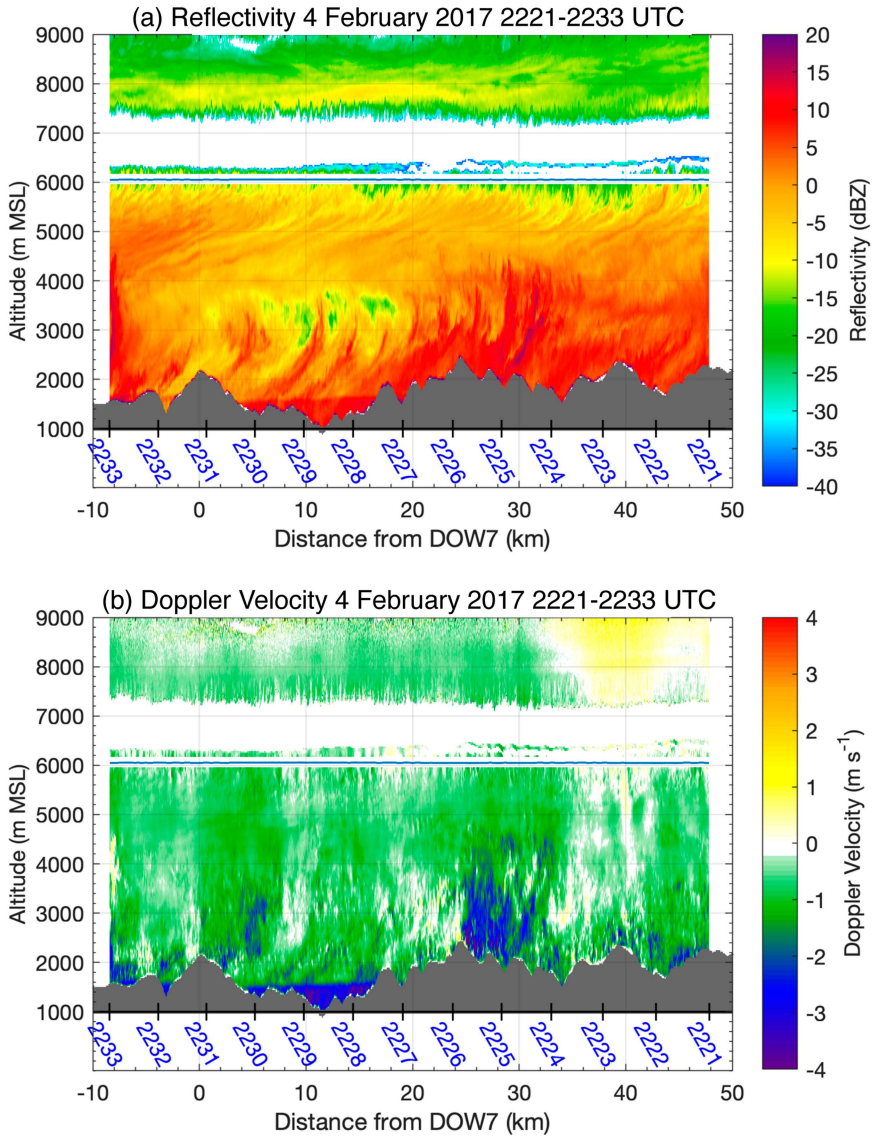

FIG. 14. As in Fig. 9, but for (a) WCR reflectivity and (b) Doppler vertical velocity along UWKA flight leg from 2221 to 2233 UTC 4 Feb 2017 (IOP11) (Fig. 1, black line).

depleting cloud water. The segment with the largest reflectivity difference inside versus outside of generating cells (22 dBZ) was 21 January 2017 starting at 2258:30 UTC (Fig. 19, PSD shown in Fig. 7b). This segment was an orographically enhanced segment with higher cloud tops than the adjacent cloud (Fig. 3b) and it had the greatest vertical velocities of all segments analyzed as well (based upon its maximum and outlier vertical velocity measurements shown in Fig. 20).

b. *Vertical air motion*

Measurements of vertical air motion from the UWKA gust probe indicated that air motions at cloud top were generally upward, especially inside generating cells (Fig. 20). The magnitude of the median vertical velocity measured at flight level was on average 0.25 m s^{-1} greater inside generating cells compared to outside the generating cells in the sampled segments. There was one segment, from 21 January 2017 starting at 2255:30 UTC, where the median vertical velocity was 0.1 m s^{-1} less inside the generating cells. Another segment starting at 2307:00 UTC 21 January 2017 exhibited negative median vertical velocity inside the generating cells, but it was still 0.02 m s^{-1} greater than the median outside the generating cells. In both of these segments, though, the 95th percentile vertical velocity inside generating cells was 0.3 and 0.7 m s^{-1}, respectively, greater than the 95th-percentile vertical velocity outside the generating cells. This analysis supports the general conclusion that the vertical velocity inside generating cells was greater than the surrounding cloudy environment. The relationship of vertical velocity to generating cell microphysics (i.e., LWC, drizzle or ice concentration) was not particularly strong in this analysis. Figure 20 is

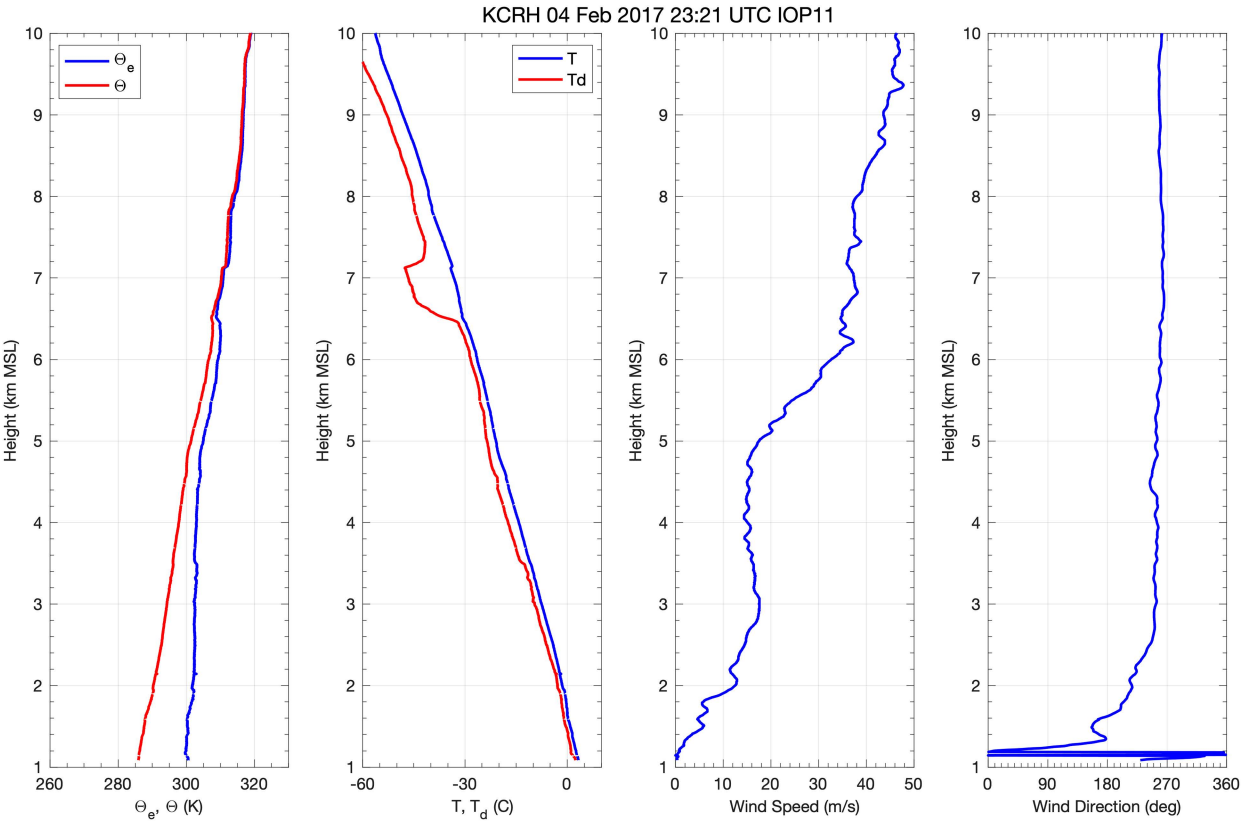

FIG. 15. Vertical profiles of thermodynamic variables from the atmospheric sounding launched at Lowman at 2321 UTC 4 Feb 2017 (IOP11). (left to right) Potential temperature (θ; K; red) and equivalent potential temperature (θ_e; K; blue), temperature (°C; blue) and dewpoint temperature (°C; red), wind speed (m s^{-1}; blue), and wind direction (°; blue), respectively.

sorted by the 2D-S ice concentration (as was Fig. 19), and there is no relationship. Rather, the vertical velocity was most related to the generating cell size (see section 6e).

c. *LWC*

The LWC (measured by the Nevzorov, which includes drop sizes up to 50 μm) was notably higher inside generating cells with less ice (Fig. 21, also sorted by 2D-S ice concentration). The LWC, especially on 21 January 2017 (IOP7) segments exhibited substantial variability from one segment to the next, but the median LWC was on average 0.15 g m^{-3} greater inside generating cells than in the adjacent cloud. The maximum difference in median LWC between inside and outside generating cells was 0.3 g m^{-3} in the segment beginning 2254:00 UTC 21 January. In the other segments analyzed (from IOP11 and IOP22), the median LWC was higher inside generating cells compared to outside, but the difference was much smaller, on average less than 0.02 g m^{-3} with the maximum difference only 0.06 g m^{-3}.

d. *Drizzle and ice*

Drizzle concentration in the generating cells was not related to the ice concentration (Fig. 22), as there were cases with drizzle with and without notable ice concentrations. The 2D-S data from the IOP11 segments, which happened to be the case with the coldest cloud-top temperature of −30°C, indicated the cloud tops were dominated by ice. While the 2D-S data indicated the presence of drizzle in the IOP11 segments, it was in low concentrations. In the segments of IOP7 and IOP22 that contained drizzle (recall both of these IOPs had warmer cloud-top temperature around −15°C), the concentration of drizzle was always greater inside generating cells (Fig. 22). The segments in IOP7 were dominated by drizzle, though a few also had ice, and when they had ice, the ice concentration was greater inside the generating cells. The segments from IOP7 that contained ice also happened to be the segments with notably higher reflectivity in the generating cells as noted previously (Fig. 19). Interestingly, in the IOP7 and IOP22 segments that had the higher LWC values, only the IOP7 segments also had high concentrations of drizzle, likely due to the lower CDP concentrations and greater cloud drop sizes in this case (Fig. 23). The IOP22A segment (1408:00 UTC 9 March) had notable drizzle, but its LWC measurements were negligible and its ice concentrations were the highest of all segments analyzed (Fig. 22). The ice formation in this segment was effectively depleting the cloud water. Another consistent observation is that the 2D-S ice particle concentrations were always greater inside generating cells than outside the generating cells (Fig. 22), but not all generating cells contained appreciable ice. In

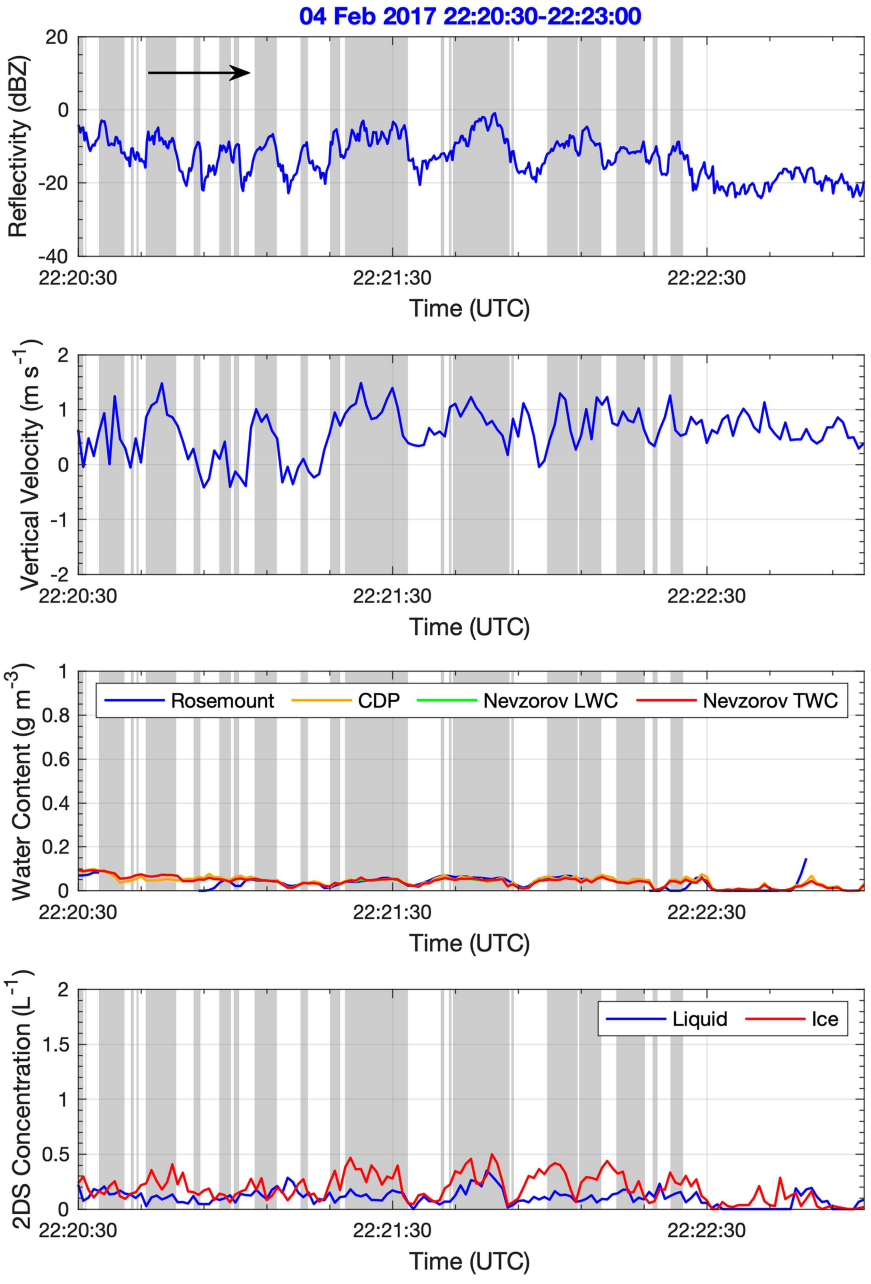

FIG. 16. Time series traces of UWKA measurements during the 2220:30–2223:00 UTC segment on 4 Feb 2017 (IOP11). (top to bottom) The WCR reflectivity (dBZ) at the nearest radar gate below the UWKA aircraft flight level, the observed vertical velocity (m s^{-1}) measured by the gust probe at the UWKA aircraft flight level, the measured water content (g m^{-3}) from the Rosemount, Nevzorov, and DMT CDP probes on the UWKA (see panel 3 legend), and the total liquid (blue) and total ice (red) concentration (L^{-1}) for particles > 100 μm as measured by the 2D-S optical array probe. The gray shading denotes times within generating cells.

segments with ice >100 μm, median concentrations were 0.08 L^{-1} greater inside generating cells, on average. While some of the segments had notable ice particle concentrations outside the generating cells as well, the concentrations were always less than in the generating cells of each of those segments.

e. *Generating cell size*

The horizontal widths of the generating cells investigated in this study were generally <500 m (Fig. 23). The mode was <100 m; however, it is likely that some of the generating cells were not sampled exactly in their center, so the high frequency

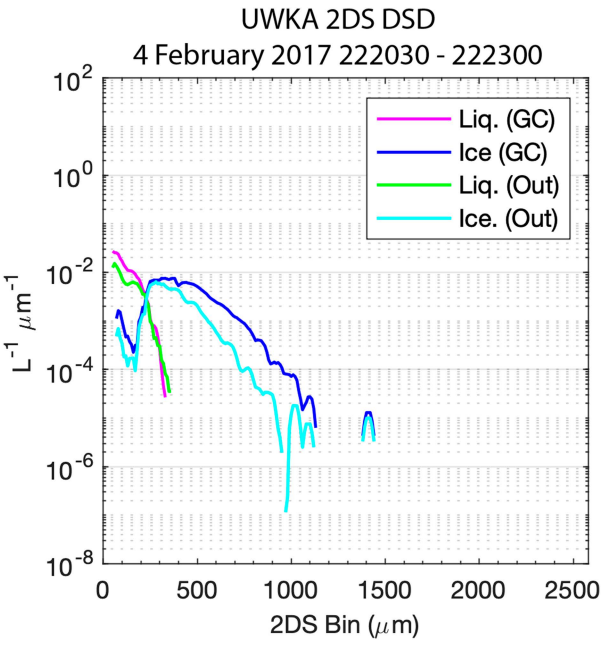

FIG. 17. Particle size distributions of 2D-S data in the 2-min segment between 2220:30 and 2233:00 UTC 4 Feb 2017 (IOP11). Magenta (liquid particles) and blue (ice particles) lines are measurements inside generating cells, while green (liquid particles) and cyan (ice particles) lines are from measurements outside generating cells.

of cells <100 m is likely due to sampling along the periphery of the cells. The median width was between 100 and 200 m, and the maximum width was 1500 m. What is clear from this analysis is that these cells are often subkilometer in scale and therefore would be undersampled by lower-resolution radars (e.g., NEXRAD). These results are consistent with those of Wang et al. (2020) that documented the majority of the generating cells sampled in clouds over the Southern Ocean were subkilometer scale, on the order of 200–600 m in that study. Other previous studies (e.g., Rosenow et al. 2014; Plummer et al. 2014; Kumjian et al. 2014) had characterized generating cells on the order of 1–2 km in midlatitude winter storms. The generating cells in these winter orographic clouds rarely had widths > 1 km.

Figure 23 also illustrates the relationship between generating cell width and multiple in situ characteristics. The width is most strongly correlated with reflectivity, and also exhibits some relationship with LWC, TWC, and vertical velocity (increasing values with increasing cell width). Given the smaller generating cells may have been flights through the periphery of larger cells, there are higher values of these parameters even for the smallest generating cells, whereas there are no large generating cells with low values of reflectivity or vertical velocity. The TWC and LWC was most strongly correlated with generating cell size in IOP7, where the least ice was observed. Once ice processes were more active, the relationship of LWC and generating cell size is not apparent (e.g., IOP11 in particular). There is not a clear relationship between generating cell size and the observed 2D-S ice concentrations (Fig. 23e). The 2D-S drizzle concentration, LWC, TWC, CDP concentration, and CDP median volume diameter (MVD) are more stratified by each IOP than generating cell size, indicating that other factors common to each case, such as cloud-top temperature and background aerosol concentrations, are important. This is especially the case for 2D-S drizzle concentration, CDP concentration, and CDP MVD, where cases with lower CDP concentration (a proxy for lower background aerosol loading) yield the largest MVD and often greater drizzle concentrations (Bernstein et al. 2019).

7. Discussion

Some of the flight segments analyzed in this study occurred in cloud tops that had a cloud layer above, while others did not. Previous studies have suggested that cloud-top radiative cooling may be a contributing, if not dominant, factor to the cloud-top instability driving the formation of cloud-top updrafts and generating cells (Rauber and Tokay 1991; Keeler et al. 2016a,b, 2017). Having an upper-level overlying cloud layer may inhibit or reduce longwave cloud-top radiative cooling, however, and all of these cases occurred during daylight hours when incoming shortwave radiation may offset longwave cloud-top cooling. This suggests that cloud-top generating cells may not require cloud-top radiative cooling for their formation. However, shallow and isolated layers of instability at cloud top were observed in all three cases, which indicates that cloud-top instability is likely important to the formation of generating cells, as has been shown in previous studies (Kumjian et al. 2014; Keeler et al. 2016b). We hypothesize that other mechanisms that may have led to the observed cloud-top instabilities could include advection of cooler air above cloud top or latent cooling processes from cloud-top entrainment. In addition, the temporal evolution of cloud-top radiative effects is another factor that needs to be considered, given shortwave and longwave radiative processes occur on different time scales, so the timing of upper-level cloud-layer advection and amounts of solar insolation need to be considered. An analysis of the environmental conditions contributing to the formation of the generating cells observed in all IOPs during SNOWIE is ongoing and will be presented in future work to better characterize the mechanisms by which these generating cells formed, and model simulations are being conducted to investigate aspects of these processes that cannot be resolved with observations alone.

The in situ measurements indicated that generating cells typically have higher LWC as well as stronger and generally upward vertical velocities; however, there are some segments analyzed that did not follow these patterns. We hypothesize that the variabilities in the vertical motions of generating cells are due to the location of the generating cells relative to the terrain-induced vertical motions, from not flying through the centers of all generating cells, and/or due to their temporal evolution (i.e., age). Several flight segments analyzed were in regions of broad upward (or downward) vertical motion tied to the terrain, as well as localized enhancements in the generating cells were observed coincident with regions of elevated terrain (e.g., IOP7 as shown in Fig. 3). Given the widespread presence of generating cells across the cloud tops (in areas of upward and downward larger-scale flow over the terrain), the terrain forcing is not likely

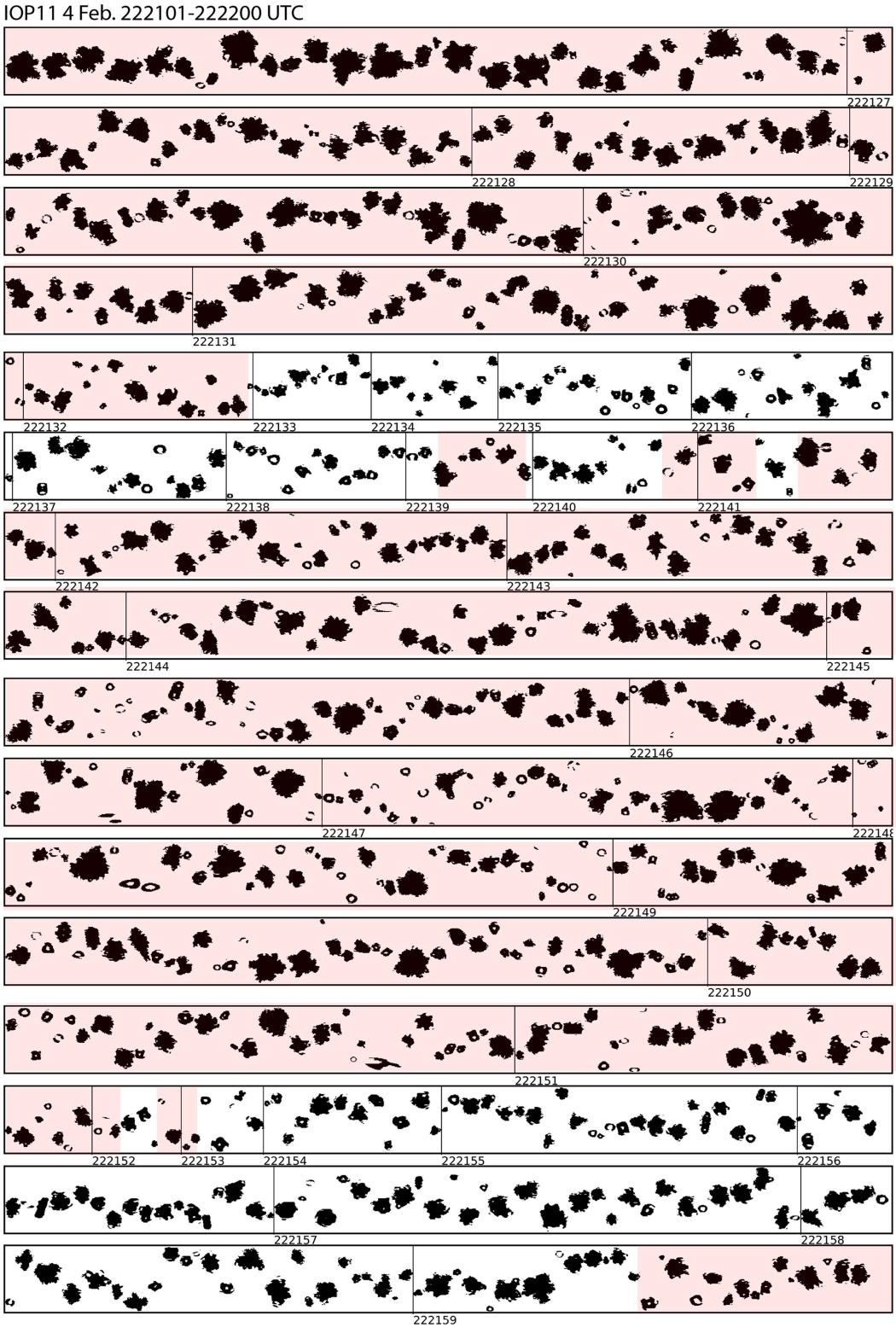

FIG. 18. 2D-S imagery >100 μm between 2221:01 and 2222:00 UTC. The red shading indicates times when the aircraft was inside generating cells. The buffer window height of each panel is 1.6 mm.

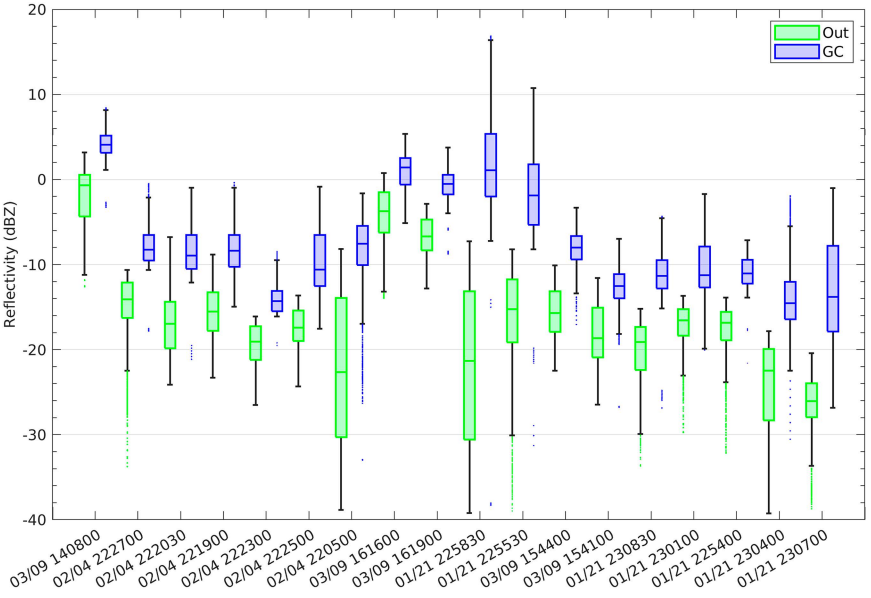

FIG. 19. Box-and-whisker plots of WCR reflectivity inside (blue) and outside (green) generating cells in seven flight segments on 21 Jan 2017 (IOP7), six segments on 4 Feb 2017 (IOP11), and five segments on 9 Mar 2017 (IOP22) in order of the generating cell median 2D-S ice concentration (shown in Fig. 22b) of each segment (highest to lowest from left to right). The starting date and time (UTC) of each segment is listed at along the x axis. Center lines indicate the median values, and the bottom and top of each box indicates the 25th and 75th percentiles, respectively. Whiskers represent ±2.7 the standard deviation of the distribution, which is 99.3% coverage if the data are normally distributed.

forcing the generating cells themselves, but may be a factor in some of their characteristics (e.g., enhanced upward motions to help nucleate and grow more ice), as is suspected in IOP7. In addition, the time evolution of the generating cell may play a role in the variability in LWC, as we have shown that generating cells with lower LWC had more ice concentration (Fig. 21), and therefore were likely more mature generating cells where ice had already effectively depleted the LWC.

Another general result was that the generating cells always exhibited greater ice concentrations compared to the interim cloudy regions between them. The ice habits observed inside generating cells were consistent with primary ice formation at the respective ambient temperatures. These results suggest that generating cells are a focal point for ice formation, which is consistent with previous studies (e.g., Marshall 1953; Ikeda et al. 2007; Plummer et al. 2014; Wang et al. 2020). We hypothesize that the environments within the generating cells provide favorable conditions for ice nucleation, perhaps due to locally enhanced supersaturations. This fine-scale variability in environmental conditions favorable for ice nucleation may also be an explanation for some of the remaining scatter shown in the INP closure studies of DeMott et al. (2010), where more INP may nucleate to form ice inside generating cells that occur at generally the same temperature and exhibit similar concentrations of particles > 0.5 μm as the adjacent portions of cloud.

However, not all generating cells exhibited large amounts of ice or ice particles >100 μm (the minimum size that 2D-S particles were categorized as ice or liquid). Minimal amounts of ice were especially noted in the low reflectivity segments in IOP7, indicating that generating cells may be detectable by high-resolution cloud radar and may not yet have active ice growth processes. IOP7 also had the lowest CDP concentrations and largest CDP MVD ($\sim$30 μm; Fig. 23), suggesting low background aerosol loading, which would favor drizzle formation (Bernstein et al. 2019). The segments that did not have appreciable ice did have drizzle and abundant supercooled cloud water (on the order of 0.2 g m^{-3} or greater). We hypothesize that these conditions may be precursors to the generating cells producing ice, and in that case suggest that, prior to ice forming, the generating cells exhibit conditions favoring enhanced supersaturation and cloud drop nucleation and growth into drizzle. The aircraft data provide an instantaneous representation of the microphysical conditions as the aircraft flew through the cloud; therefore, they do not allow us to study the temporal evolution of generating cells to confirm this hypothesis. It is also possible that the freezing of drizzle drops formed in generating cells may lead to secondary ice production (e.g., Lauber et al. 2018; Keinert et al. 2020; Korolev and Leisner 2020; Kleinheins et al. 2021; Luke et al. 2021); however, this cannot be determined with the given dataset due to the inability to distinguish ice particles < 100 μm in size and a lack of INP measurements.

The variability in the measured conditions within generating cells may also be a factor of the amount of mixing that the generating cells have been subjected to. As noted in Wang et al. (2020), mixing processes may reduce the distinction between generating cells and the surrounding cloud over time as the generating cells

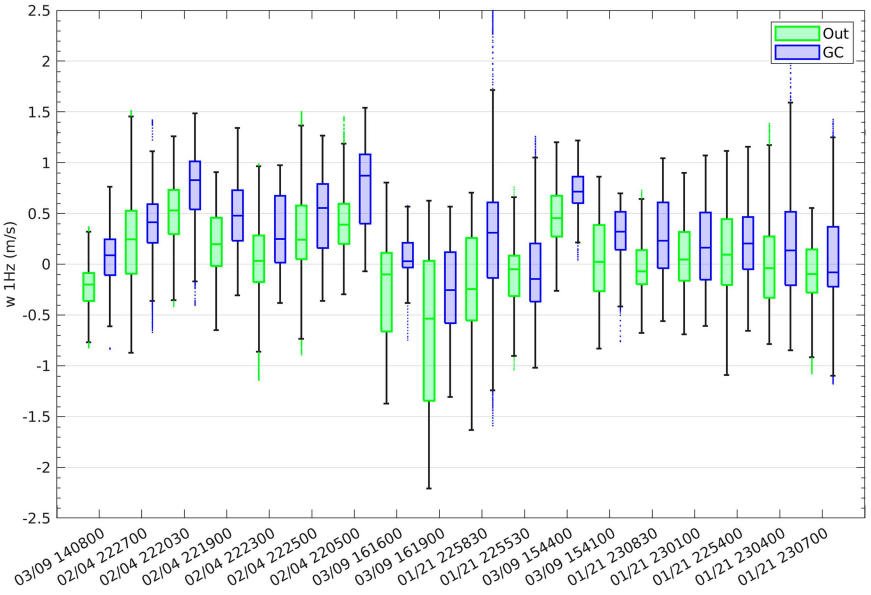

FIG. 20. As in Fig. 19, but for vertical velocity inside (blue) and outside (green) generating cells.

become "older." We hypothesize, however, that in clouds where generating cells are just starting to form that their characteristics may be less distinct from the surrounding cloud until they have had time to form and grow enhanced amounts of drizzle and ice. This hypothesis is supported by temporal evolution of IOP22 in the flight legs shown in Fig. 15, where the cloud-top LWC and microphysical conditions at 1541:00 and 1544:00 UTC were less distinct from the surrounding cloud as in the segments at 1616:00 and 1619:00 UTC where more drizzle and ice was present (Figs. 19–22). Without being able to track and resolve the time evolution or age of individual generating cells, we cannot explain all of the observed variability and model simulations are needed to further test these hypotheses. Moreover, untangling the terrain effects on generating cells is not possible with the observations alone. Numerical modeling studies are underway to investigate the temporal evolution of microphysics in generating cells (Chen et al. 2023) as well as study the effect of underlying terrain.

8. Summary

Cloud-top generating cells were frequently observed in winter orographic clouds during the SNOWIE field campaign via the

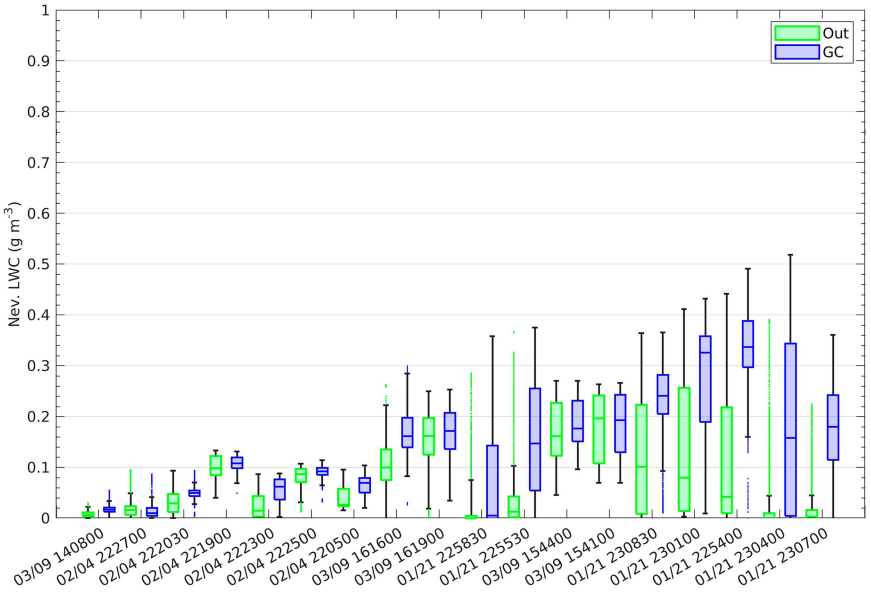

FIG. 21. As in Fig. 19, but for liquid water content from the Nevzorov probe inside (blue) and outside (green) generating cells.

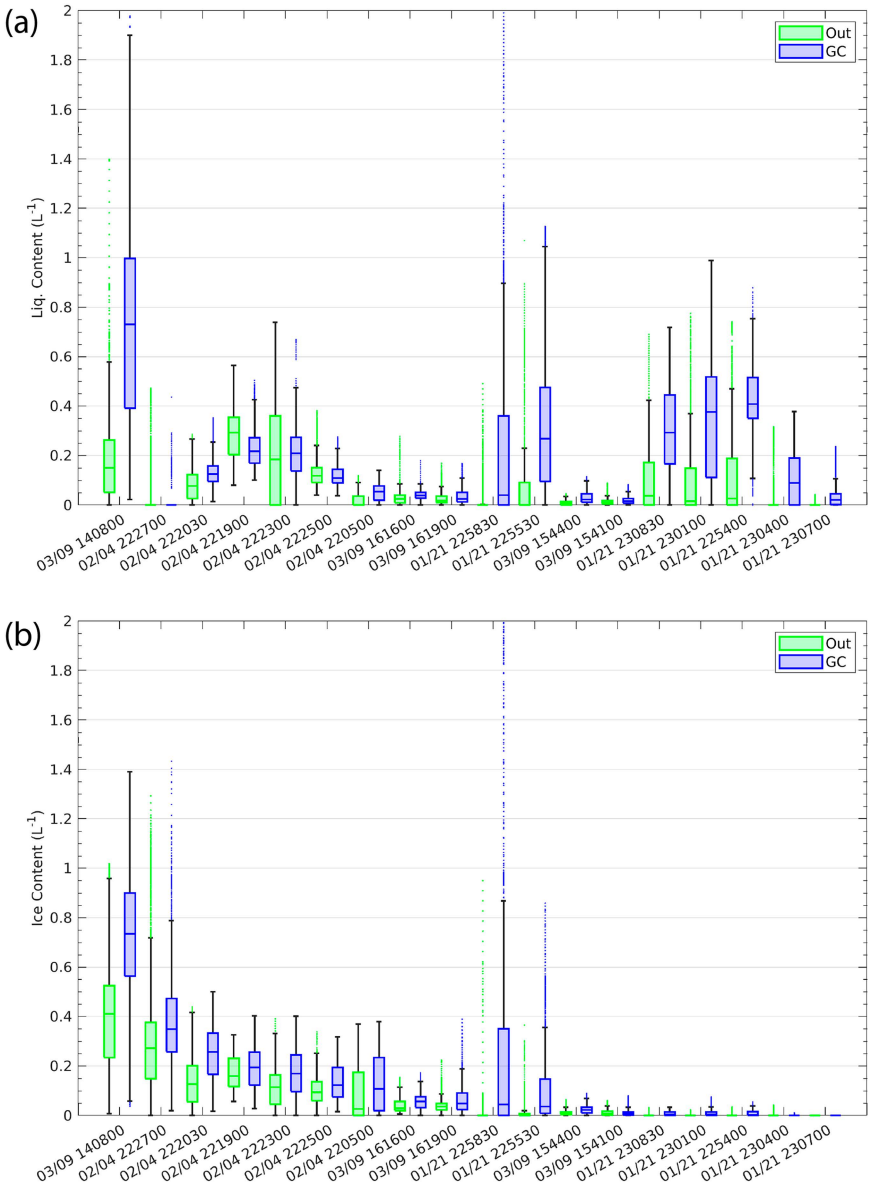

FIG. 22. As in Fig. 19, but for (a) drizzle concentration and (b) ice concentration inside (blue) and outside (green) generating cells, as measured by the 2D-S for particles > 100 μm.

W-band radar on board the UWKA. In this study, in situ measurements were analyzed using the radar and other in situ aircraft data from the three IOPs when the UWKA flew through the tops of the generating cells. Cloud-top temperatures ranged from as warm as -15°C to as cold as -30°C in these three cases. This study documented that cloud-top generating cells in SNOWIE occurred in orographic clouds with and without overlying cloud layers and at altitudes with shallow layers of atmospheric instability.

Generating cells were shown to have enhanced vertical velocity and be focal points for enhanced LWC and drizzle growth, as well as ice formation and growth. When ice concentrations were higher, LWC was reduced at the expense of the ice growth. This study adds to the growing number of studies documenting that cloud-top generating cells are ubiquitous, herein documenting them in winter orographic clouds and in clouds with and without overlying cloud layers, and they play a role in precipitation formation. Specifically, they provide environments conducive to ice formation and growth on subkilometer scales, which is often unresolved by operational observational networks and numerical weather prediction models.

This study reaffirms that studies of precipitation and ice formation need high-resolution radar measurements to be able to detect the presence of generating cells. Furthermore, it may be important for numerical model parameterizations

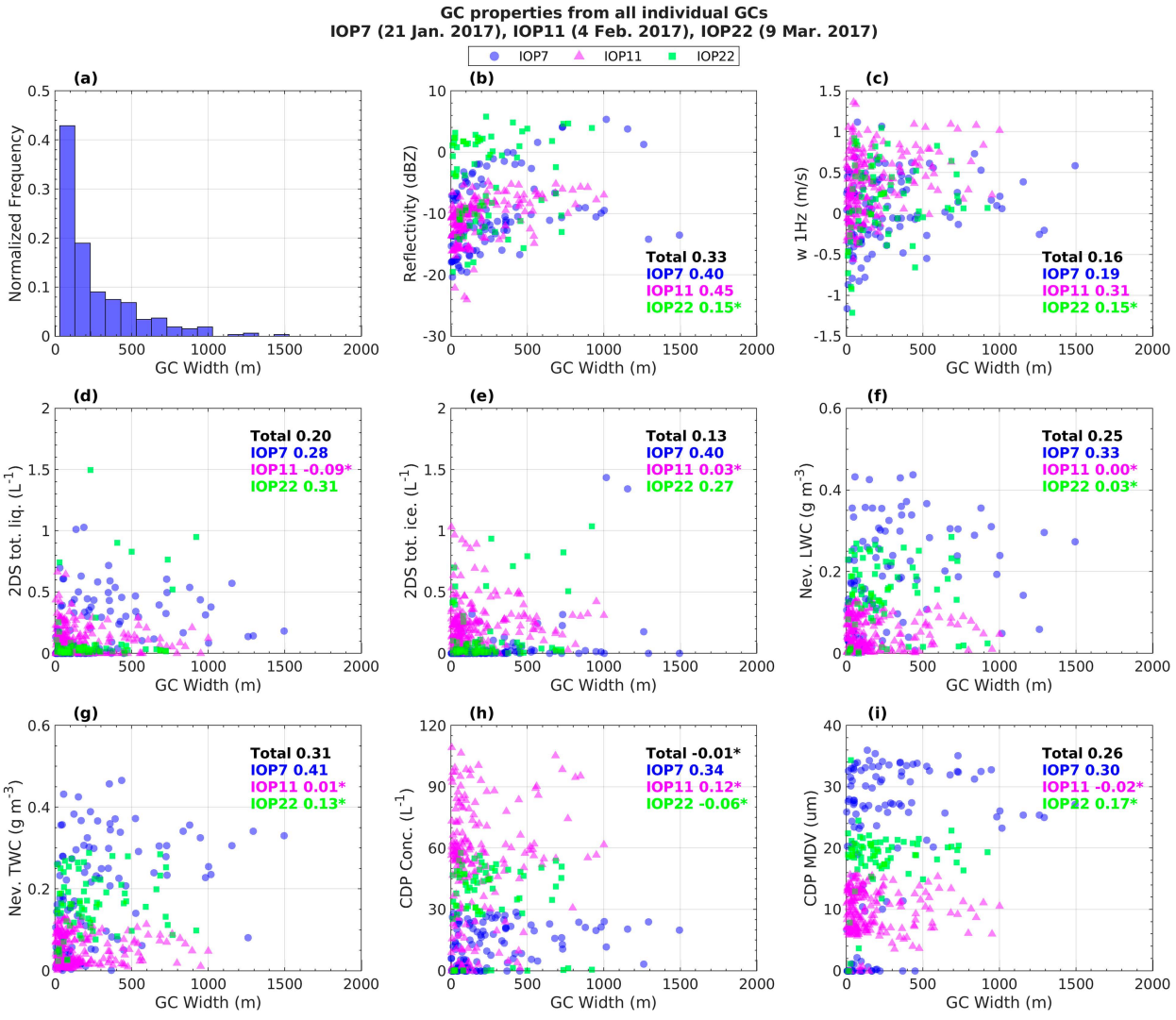

FIG. 23. (a) Normalized histogram of generating cell widths for all analyzed segments in the three IOPs studied, and scatterplots of generating cell width vs mean in situ measurements inside each generating cell: (b) WCR reflectivity, (c) vertical velocity, (d) 2D-S liquid concentration > 100 μm, (e) 2D-S ice concentration >100 μm, (f) Nevzorov LWC, (g) Nevzorov TWC, (h) CDP concentration, and (i) CDP MDV. The scatterplots are colored by IOP, and include Pearson correlation coefficients for all data points (black), and for data points by IOP (color matches IOP color).

of ice nucleation to consider subkilometer generating cells as a factor in precipitation formation, especially in order to better represent natural ice phase microphysical processes since many model simulations, such as those used for operational numerical weather prediction, are run at too coarse of grid spacing to resolve these fine-scale circulations.

Acknowledgments. The authors thank Jamie Wolff and Cindy Halley Gotway for editorial and graphics support. We would also like to thank the crew from the UWKA as well as all students from the Universities of Colorado, Wyoming, and Illinois for their help operating and deploying instruments during the SNOWIE campaign. Funding for the UWKA was provided through the National Science Foundation (NSF) Grant AGS-1441831. The research was supported under NSF Grants AGS-1547101, AGS-1546963, AGS-1546939, and by Idaho Power Company. This material is based upon work supported by the National Center for Atmospheric Research, which is a major facility sponsored by the National Science Foundation under Cooperative Agreement 1852977.

Data availability statement. All data presented here are publicly available through the SNOWIE data archive website (https://data.eol.ucar.edu/master_lists/generated/snowie/) maintained by the Earth Observing Laboratory (EOL) at the National Center for Atmospheric Research (NCAR).

REFERENCES

American Meteorological Society, 2023: Generating cell. Glossary of Meteorology, https://glossary.ametsoc.org/wiki/Generating_cell.

Bailey, M. P., and J. Hallett, 2009: A comprehensive habit diagram for atmospheric ice crystals: Confirmation from the laboratory, AIRS II, and other field studies. *J. Atmos. Sci.*, **66**, 2888–2899, https://doi.org/10.1175/2009JAS2883.1.

Bergeron, T., 1935: On the physics of cloud and precipitation. *Proc. Fifth Assembly of the Int. Union of Geodesy and Geophysics*, Lisbon, Portugal, UGGI, 156–173.

Bernstein, B. C., R. M. Rasmussen, F. McDonough, and C. Wolff, 2019: Keys to differentiating between small- and large-drop icing conditions in continental clouds. *J. Appl. Meteor. Climatol.*, **58**, 1931–1953, https://doi.org/10.1175/JAMC-D-18-0038.1.

Carbone, R. E., and A. R. Bohne, 1975: Cellular snow generation—A Doppler radar study. *J. Atmos. Sci.*, **32**, 1384–1394, https://doi.org/10.1175/1520-0469(1975)032<1384:CSGDRS>2.0.CO;2.

Chen, S., and Coauthors, 2023: Mixed-phase direct numerical simulation: Ice growth in cloud-top generating cells. *Atmos. Chem. Phys.*, **23**, 5217–5231, https://doi.org/10.5194/acp-23-5217-2023.

Ciesielski, P. E., P. T. Haertel, R. H. Johnson, J. Wang, and S. M. Loehrer, 2012: Developing high-quality field program sounding datasets. *Bull. Amer. Meteor. Soc.*, **93**, 325–336, https://doi.org/10.1175/BAMS-D-11-00091.1.

DeMott, P. J., and Coauthors, 2010: Predicting global atmospheric ice nuclei distributions and their impact on climate. *Proc. Natl. Acad. Sci. USA*, **107**, 11 217–11 222, https://doi.org/10.1073/pnas.0910818107.

Evans, A. G., J. D. Locatelli, M. T. Stoelinga, and P. V. Hobbs, 2005: The IMPROVE-1 storm of 1–2 February 2001. Part II: Cloud structures and the growth of precipitation. *J. Atmos. Sci.*, **62**, 3456–3473, https://doi.org/10.1175/JAS3547.1.

Faber, S., J. R. French, and R. Jackson, 2018: Laboratory and in-flight evaluation of measurement uncertainties from a commercial Cloud Droplet Probe (CDP). *Atmos. Meas. Tech.*, **11**, 3645–3659, https://doi.org/10.5194/amt-11-3645-2018.

Field, P. R., and Coauthors, 2017: Secondary ice production: Current state of the science and recommendations for the future. *Ice Formation and Evolution in Clouds and Precipitation: Measurement and Modeling Challenges*, *Meteor. Monogr.*, No. 58, Amer. Meteor. Soc., https://doi.org/10.1175/AMSMONOGRAPHS-D-16-0014.1.

Findeisen, W., 1938: Die kolloidmeteorologischen Vorgänge bei der Niederschlagsbildung (Colloidal meteorological processes in the formation of precipitation). *Meteor. Z.*, **55**, 121–133.

Fletcher, N. H., 1962: *The Physics of Rain Clouds*. Cambridge University Press, 386 pp.

Hallett, J., and S. C. Mossop, 1974: Production of secondary ice particles during the riming process. *Nature*, **249**, 26–28, https://doi.org/10.1038/249026a0.

Hobbs, P. V., T. J. Matejka, P. H. Herzegh, J. D. Locatelli, and R. A. Houze Jr., 1980: The mesoscale and microscale structure and organization of clouds and precipitation in midlatitude cyclones. I: A case study of a cold front. *J. Atmos. Sci.*, **37**, 568–596, https://doi.org/10.1175/1520-0469(1980)037<0568:TMAMSA>2.0.CO;2.

Houze, R. A., Jr., S. A. Rutledge, T. J. Matejka, and P. V. Hobbs, 1981: The mesoscale and microscale structure and organization of clouds and precipitation in midlatitude cyclones. III: Air motions and precipitation growth in a warm-frontal rainband. *J. Atmos. Sci.*, **38**, 639–649, https://doi.org/10.1175/1520-0469(1981)038<0639:TMAMSA>2.0.CO;2.

Ikeda, K., R. M. Rasmussen, W. D. Hall, and G. Thompson, 2007: Observations of freezing drizzle in extratropical cyclonic storms during IMPROVE-2. *J. Atmos. Sci.*, **64**, 3016–3043, https://doi.org/10.1175/JAS3999.1.

Keeler, J. M., B. F. Jewett, R. M. Rauber, G. M. McFarquhar, R. M. Rasmussen, L. Xue, C. Liu, and G. Thompson, 2016a: Dynamics of cloud-top generating cells in winter cyclones. Part I: Idealized simulations in the context of field observations. *J. Atmos. Sci.*, **73**, 1507–1527, https://doi.org/10.1175/JAS-D-15-0126.1.

——, ——, ——, ——, ——, ——, ——, and ——, 2016b: Dynamics of cloud-top generating cells in winter cyclones. Part II: Radiative and instability forcing. *J. Atmos. Sci.*, **73**, 1529–1553, https://doi.org/10.1175/JAS-D-15-0127.1.

——, ——, ——, ——, ——, ——, ——, and ——, 2017: Dynamics of cloud-top generating cells in winter cyclones. Part III: Shear and convective organization. *J. Atmos. Sci.*, **74**, 2879–2897, https://doi.org/10.1175/JAS-D-16-0314.1.

Keinert, A., D. Spannagel, T. Leisner, and A. Kiselev, 2020: Secondary ice production upon freezing of freely falling drizzle droplets. *J. Atmos. Sci.*, **77**, 2959–2967, https://doi.org/10.1175/JAS-D-20-0081.1.

Kleinheins, J., A. Kiselev, A. Keinert, M. Kind, and T. Leisner, 2021: Thermal imaging of freezing drizzle droplets: Pressure release events as a source of secondary ice particles. *J. Atmos. Sci.*, **78**, 1703–1713, https://doi.org/10.1175/JAS-D-20-0323.1.

Korolev, A., and P. R. Field, 2015: Assessment of the performance of the inter-arrival time algorithm to identify ice shattering artifacts in cloud particle probe measurements. *Atmos. Meas. Tech.*, **8**, 761–777, https://doi.org/10.5194/amt-8-761-2015.

——, and T. Leisner, 2020: Review of experimental studies of secondary ice production. *Atmos. Chem. Phys.*, **20**, 11 767–11 797, https://doi.org/10.5194/acp-20-11767-2020.

——, E. Emery, and K. Creelman, 2013: Modification and tests of particle probe tips to mitigate effects of ice shattering. *J. Atmos. Oceanic Technol.*, **30**, 690–708, https://doi.org/10.1175/JTECH-D-12-00142.1.

Kumjian, M. R., S. A. Rutledge, R. M. Rasmussen, P. C. Kennedy, and M. Dixon, 2014: High-resolution polarimetric radar observations of snow-generating cells. *J. Appl. Meteor. Climatol.*, **53**, 1636–1658, https://doi.org/10.1175/JAMC-D-13-0312.1.

Lance, S., C. Brock, D. Rogers, and J. A. Gordon, 2010: Water droplet calibration of the Cloud Droplet Probe (CDP) and in-flight performance in liquid, ice and mixed-phase clouds during ARCPAC. *Atmos. Meas. Tech.*, **3**, 1683–1706, https://doi.org/10.5194/amt-3-1683-2010.

Lauber, A., A. Kiselev, T. Pander, P. Handmann, and T. Leisner, 2018: Secondary ice formation during freezing of levitated droplets. *J. Atmos. Sci.*, **75**, 2815–2826, https://doi.org/10.1175/JAS-D-18-0052.1.

Lawson, R. P., D. O'Connor, P. Zmarzly, K. Weaver, B. A. Baker, Q. Mo, and H. Jonsson, 2006: The 2D-S (stereo) probe: Design and preliminary tests of a new airborne, high-speed, high-resolution particle imaging probe. *J. Atmos. Oceanic Technol.*, **23**, 1462–1477, https://doi.org/10.1175/JTECH1927.1.

Luke, E. P., F. Yang, P. Kollias, A. M. Vogelmann, and M. Maahn, 2021: New insights into ice multiplication using remote-sensing observations of slightly supercooled mixed-phase clouds in the Arctic. *Proc. Natl. Acad. Sci. USA*, **118**, e2021387118, https://doi.org/10.1073/pnas.2021387118.

Magono, C., and C. W. Lee, 1966: Meteorological classification of natural snow crystals. *J. Fac. Sci. Hokkaido Univ. Ser. 7*, **2**, 321–335.

Marshall, J. S., 1953: Precipitation trajectories and patterns. *J. Meteor.*, **10**, 25–29, https://doi.org/10.1175/1520-0469(1953)010<0025:PTAP>2.0.CO;2.

McFarquhar, G. M., and Coauthors, 2011: Indirect and Semi-Direct Aerosol Campaign: The impact of Arctic aerosols on clouds. *Bull. Amer. Meteor. Soc.*, **92**, 183–201, https://doi.org/10.1175/2010BAMS2935.1.

Meyers, M. P., P. J. DeMott, and W. R. Cotton, 1992: New primary ice-nucleation parameterizations in an explicit cloud model. *J. Appl. Meteor.*, **31**, 708–721, https://doi.org/10.1175/1520-0450(1992)031<0708:NPINPI>2.0.CO;2.

Plummer, D. M., G. M. McFarquhar, R. M. Rauber, B. F. Jewett, and D. C. Leon, 2014: Structure and statistical analysis of the microphysical properties of generating cells in the comma head region of continental winter cyclones. *J. Atmos. Sci.*, **71**, 4181–4203, https://doi.org/10.1175/JAS-D-14-0100.1.

——, ——, ——, ——, and ——, 2015: Microphysical properties of convectively generated fall streaks within the stratiform comma head region of continental winter cyclones. *J. Atmos. Sci.*, **72**, 2465–2483, https://doi.org/10.1175/JAS-D-14-0354.1.

Pruppacher, H. R., and J. D. Klett, 1997: *Microphysics of Clouds and Precipitation*. Kluwer Academic, 954 pp.

Rauber, R. M., and A. Tokay, 1991: An explanation for the existence of supercooled water at the top of cold clouds. *J. Atmos. Sci.*, **48**, 1005–1023, https://doi.org/10.1175/1520-0469(1991)048<1005:AEFTEO>2.0.CO;2.

——, M. K. Macomber, D. M. Plummer, A. A. Rosenow, G. M. McFarquhar, B. F. Jewett, D. Leon, and J. M. Keeler, 2014: Finescale radar and airmass structure of the comma head of a continental winter cyclone: The role of three airstreams. *Mon. Wea. Rev.*, **142**, 4207–4229, https://doi.org/10.1175/MWR-D-14-00057.1.

——, and Coauthors, 2015: The role of cloud-top generating cells and boundary layer circulations in the finescale radar structure of a winter cyclone over the Great Lakes. *Mon. Wea. Rev.*, **143**, 2291–2318, https://doi.org/10.1175/MWR-D-14-00350.1.

——, S. M. Ellis, J. Vivekanandan, J. Stith, W.-C. Lee, G. M. McFarquhar, B. F. Jewett, and A. Janiszeski, 2017: Finescale structure of a snowstorm over the northeastern United States: A first look at high-resolution HIAPER cloud radar observations. *Bull. Amer. Meteor. Soc.*, **98**, 253–269, https://doi.org/10.1175/BAMS-D-15-00180.1.

Rosenow, A. A., D. M. Plummer, R. M. Rauber, G. M. McFarquhar, B. F. Jewett, and D. Leon, 2014: Vertical velocity and physical structure of generating cells and convection in the comma head region of continental winter cyclones. *J. Atmos. Sci.*, **71**, 1538–1558, https://doi.org/10.1175/JAS-D-13-0249.1.

Tessendorf, S. A., and Coauthors, 2019: Transformational approach to winter orographic weather modification research: The SNOWIE project. *Bull. Amer. Meteor. Soc.*, **100**, 71–92, https://doi.org/10.1175/BAMS-D-17-0152.1.

——, and Coauthors, 2021: Differentiating freezing drizzle and freezing rain in HRRR model forecasts. *Wea. Forecasting*, **36**, 1237–1251, https://doi.org/10.1175/WAF-D-20-0138.1.

Wang, Y., and Coauthors, 2020: Microphysical properties of generating cells over the Southern Ocean: Results from SOCRATES. *J. Geophys. Res. Atmos.*, **125**, e2019JD032237, https://doi.org/10.1029/2019JD032237.

Wang, Z., and Coauthors, 2012: Single aircraft integration of remote sensing and in situ sampling for the study of cloud microphysics and dynamics. *Bull. Amer. Meteor. Soc.*, **93**, 653–668, https://doi.org/10.1175/BAMS-D-11-00044.1.

Wegener, A., 1911: *Thermodynamik der Atmosphäre*. Barth, 331 pp.

Wexler, R., and D. Atlas, 1959: Precipitation generating cells. *J. Meteor.*, **16**, 327–332, https://doi.org/10.1175/1520-0469(1959)016<0327:PGC>2.0.CO;2.

Zaremba, T. J., and Coauthors, 2022: Vertical motions in orographic cloud systems over the Payette River basin. Part II: Fixed and transient updrafts and their relationship to forcing. *J. Appl. Meteor. Climatol.*, **61**, 1733–1751, https://doi.org/10.1175/JAMC-D-21-0229.1.